Electronic supplementary material

Breaking a Molecular Scaling Relationship Using an Iron-Iron Fused Porphyrin Electrocatalyst for Oxygen Reduction

Daiki Nishiori,[1,2] Jan Paul Menzel,[3] Nicholas Armada,[1,2] Edgar A. Reyes Cruz,[1,2] Brent L. Nannenga,[2,4] Victor S. Batista,[3,5] and Gary F. Moore*[1,2]

[1]School of Molecular Sciences, Arizona State University, Tempe, AZ 85287-1604, United States

[2]Center for Applied Structural Discovery (CASD), The Biodesign Institute, Arizona State University, Tempe, AZ 85281, United States

[3]Department of Chemistry, Yale University, New Haven, CT 06520-8107, United States

[4]Chemical Engineering, School for Engineering of Matter, Transport and Energy, Arizona State University, Tempe, AZ 85287, United States

[5]Energy Sciences Institute, Yale University, West Haven, CT 06516, United States

gfmoore@asu.edu

Index

1. Molecular structures

Chart S1. Molecular structures of $[Fe_2FP]Cl_2$, [FeTTP]Cl, [FeT*p*CF_3PP]Cl, and [FeT*p*OMePP]Cl.

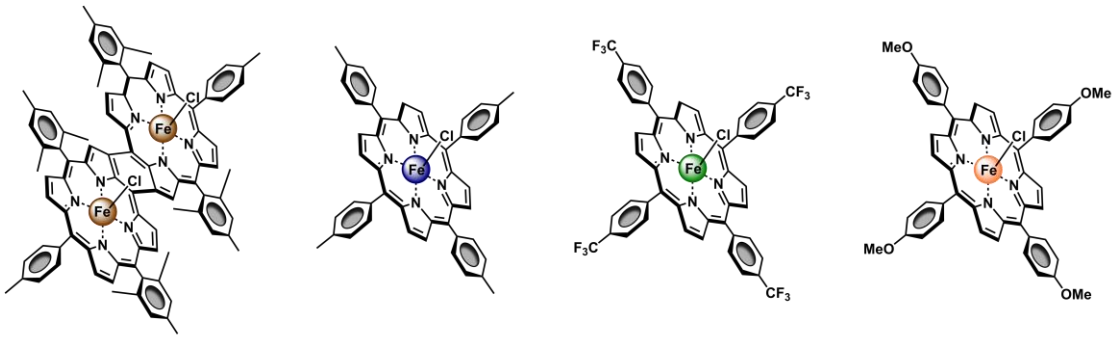

The application of ligands featuring π-extended macrocycles—as exemplified herein using the fused porphyrin, $[Fe_2FP]Cl_2$, versus the non-fused model compounds, [FeTTP]Cl, [FeT*p*CF_3PP]Cl, and [FeT*p*OMePP]Cl—provides a promising line of action to improve a catalyst's nucleophilic and electrophilic character. Experimental evidence supporting this approach includes studies involving benzene, naphthalene, and anthracene which display increasing ease of reduction (electrophilicity) and increasing basicity (nucleophilicity). Naphthalene is reduced by sodium and amyl alcohol to tetra-hydronaphthalene, whereas benzene is unattacked by these reagents.[1] Juxtaposed, naphthalene is ~10,000 times more basic than benzene, and anthracene is ~10,000,000 times more basic than naphthalene.[2]

2. Molecular synthesis and characterization

2.1. Synthesis

$[Fe_2FP]Cl_2$ was synthesized using a modified version of a reported method.[3] $FeCl_2{\cdot}4H_2O$ (41.8 mg, 0.210 mmol) was added in approximately three equivalent portions over 30 min to a refluxing solution of *meso*-β doubly-fused 5,24-di-(*p*-tolyl)-10,19,29-38-tetramesitylporphyrin (FP) (27.8 mg, 0.0219 mmol) in *N*,*N'*-dimethylformamide (13.9 mL). The crude product was purified via column chromatography using alumina as the stationary phase and 50:50:3 dichloromethane:hexane:methanol as the mobile phase. The dark purple fractions eluted from the column were concentrated under reduced pressure before redissolving in dichloromethane and washing with an aqueous 6 M hydrochloric acid solution using a separatory funnel. Collection of the organic phase and solvent removal under reduced pressure gave the target compound a near quantitative (97%) yield. For MicroED analysis, a sample of $[Fe_2FP]Cl_2$ was recrystallized from dichloromethane/acetonitrile to give a powdered sample. UV−vis (dichloromethane) 375 nm, 410 nm, 499 nm, 532 nm, 681 nm, 737 nm, 790 nm, 895 nm; FTIR (KBr) 1498 cm^{-1}, 1463 cm^{-1}, 1378 cm^{-1}, 1321 cm^{-1}, 1208 cm^{-1}, 1182 cm^{-1}, 1162 cm^{-1}, 1109 cm^{-1}, 1065 cm^{-1}, 1001 cm^{-1}; MALDI-TOF MS m/z calcd. for $C_{90}H_{72}Cl_2Fe_2N_8$ 1446.396, obsd. 1446.9.

5,10,15,20-tetrakis[4-(trifluoromethyl)phenyl]porphyrin (T*p*CF_3PP) was synthesized via condensation of pyrrole with 4-(trifluoromethyl)benzaldehyde in the presence of BF_3 diethyl etherate ($BF_3{\cdot}OEt_2$) using the

Lindsey method.[4,5] A solution of 400 mL chloroform with 4-trifluoromethyl benzaldehyde (494 mg, 2.84 mmol) and freshly distilled pyrrole (190.5 mg, 2.84 mmol) was degassed with a stream of argon for 15 min before adding $BF_3 \cdot OEt_2$ (134 mg, 0.946 mmol) using a syringe. After stirring the mixture overnight, 2,3-dichloro-5,6-dicyano-1,4-benzoquinone (DDQ) (486 mg, 2.14 mmol) was added and the mixture was stirred for 4 h. Solvent was evaporated at reduced pressure and the crude product was purified via column chromatography on silica using chloroform:hexanes = 1:1 as the eluent. Recrystallization from chloroform/methanol gave 366 mg of the desired porphyrin as a purple crystalline solid (10% yield). ^{1}H NMR (400 MHz, $CDCl_3$): δ –2.84 (2H, s, NH), 8.05 (8H, d, J = 8.0 Hz, ArH), 8.34 (8H, d, J = 7.9 Hz, ArH), 8.81 (8H, s, βH); UV−vis (dichloromethane) 417 nm, 513 nm, 547 nm, 588 nm, 643 nm; FTIR (KBr) 1474 cm^{-1}, 1406 cm^{-1}, 1324 cm^{-1}, 1224 cm^{-1}, 1215 cm^{-1}, 1169 cm^{-1}, 1127 cm^{-1}, 1107 cm^{-1}, 1068 cm^{-1}, 1021 cm^{-1}, 995 cm^{-1}, 981 cm^{-1}, 968 cm^{-1}, 957 cm^{-1}; MALDI-TOF MS m/z calcd. for $C_{48}H_{26}F_{12}N_4$ 886.197, obsd. 886.3.

Chloro[5,10,15,20-tetrakis[4-(trifluoromethyl)phenyl]porphyrinato]iron(III) ([FeT*p*CF_3PP]Cl) was synthesized following a modified version of a reported method.[6] $FeCl_2 \cdot 4H_2O$ (53.8 mg, 0.271 mmol) was added in approximately three equivalent portions over 30 min to a refluxing solution of T*p*CF_3PP (50.0 mg, 0.0564 mmol) in *N*,*N'*-dimethylformamide (25.7 mL). The crude compound was purified via column chromatography using alumina (activated basic) as the stationary phase and dichloromethane containing 3% methanol as the mobile phase. The green fraction eluted from the column was concentrated under reduced pressure before redissolving in dichloromethane and stirring with an aqueous 6 M hydrochloric acid solution for an hour. After collecting the organic phase and removing the solvent at reduced pressure, the compound was recrystallized from dichloromethane/hexanes to give 18.1 mg of the target compound as a purple crystalline solid (33% yield). UV−vis (dichloromethane) 374 nm, 416 nm, 508 nm, 575 nm, 654 nm, 679 nm; FTIR (KBr) 1473 cm^{-1}, 1463 cm^{-1}, 1404 cm^{-1}, 1324 cm^{-1}, 1167 cm^{-1}, 1127 cm^{-1}, 1107 cm^{-1}, 1068 cm^{-1}, 1022 cm^{-1}, 999 cm^{-1}; MALDI-TOF MS m/z calcd. for $C_{48}H_{24}ClF_{12}FeN_4$ 975.085, obsd. 975.1.

5,10,15,20-tetrakis(4-methoxyphenyl)porphyrin (T*p*OMePP) was synthesized via condensation of pyrrole with 4-(methoxy)benzaldehyde in refluxing propionic acid using a modified version of the Adler-Longo method.[7] Equimolar loadings of pyrrole (335.45 mg, 5 mmol) and 4-methoxybenzaldehyde (680.75 mg, 5 mmol) were refluxed in propionic acid (12.5 mL) for 30 minutes. The resulting precipitate was collected via vacuum filtration and rinsed with cold methanol. After drying, the remaining solid was redissolved in chloroform (75 mL) and subsequently reacted with DDQ (249.7 mg, 1.10 mmol) for 3 h at 40 °C to oxidize chlorin impurities.[8] After the reaction mixture cooled to room temperature, triethylamine (7.45 g, 6.66 mmol) was added to quench excess DDQ. The solution was filtered through an alumina plug to remove any remaining DDQ and concentrated *in vacuo*. The purple residue was purified via column chromatography on alumina using a mixture of dichloromethane:hexanes (1:1) as the eluent and was subsequently recrystallized from chloroform/methanol to afford 144.5 mg of the target compound as dark violet crystals (4% yield). ^{1}H NMR (400 MHz, $CDCl_3$): δ –2.75 (2H, s, NH), 4.10 (12H, s, OCH_3), 7.29 (8H, d, J = 8.5 Hz, ArH), 8.13 (8H, d, J = 8.5 Hz, ArH), 8.86 (8H, s, βH); UV−vis (dichloromethane) 422 nm, 519 nm, 556 nm, 594 nm, 650 nm; FTIR (KBr) 1509 cm^{-1}, 1471 cm^{-1}, 1441 cm^{-1}, 1410 cm^{-1}, 1384 cm^{-1}, 1351 cm^{-1}, 1289 cm^{-1}, 1248 cm^{-1}, 1175 cm^{-1}, 1156 cm^{-1}, 1107 cm^{-1}, 1072 cm^{-1}, 1035 cm^{-1}, 983 cm^{-1} 967 cm^{-1}; MALDI-TOF MS m/z calcd. for $C_{48}H_{38}N_4O_4$ 734.289, obsd. 734.4.

5,10,15,20-tetrakis(4-methoxyphenyl)porphyrin ([FeT*p*OMePP]Cl) was synthesized following a modified version of a reported method.[9] $FeCl_2 \cdot 4H_2O$ (1004.3 mg, 5.051 mmol) was added in approximately three equivalent portions over 30 min to a refluxing solution of T*p*OMePP (116.1 mg, 0.158 mmol) in *N*,*N'*-dimethylformamide (11.5 mL). The reaction was stirred for 3 h and subsequently diluted with 27 mL of chloroform. The solution was washed with aqueous 1 M hydrochloric acid three times and with water twice. The solvent was removed *in vacuo* and the crude residue was purified via column chromatography using alumina as the stationary phase and 4:1 dichloromethane:hexanes as the mobile phase. The green residue eluted from the column was concentrated *in vacuo*, redissolved in dichloromethane, and washed with aqueous 6 M hydrochloric acid in a separatory funnel. After collecting the organic phase and removing the solvent *in vacuo*, the compound was recrystallized from dichloromethane/methanol to give the target compound in 43% yield. UV−vis (dichloromethane) 386 nm, 422 nm, 513 nm, 706 nm; FTIR (KBr) 1528 cm^{-1}, 1512 cm^{-1}, 1495 cm^{-1}, 1463 cm^{-1}, 1439 cm^{-1}, 1385 cm^{-1}, 1340 cm^{-1}, 1336 cm^{-1}, 1289 cm^{-1}, 1249 cm^{-1}, 1203 cm^{-1}, 1176 cm^{-1}, 1107 cm^{-1}, 1071 cm^{-1}, 1034 cm^{-1}, 1024 cm^{-1}, 997 cm^{-1}; MALDI-TOF MS m/z calcd. for $C_{48}H_{24}ClF_{12}FeN_4$ 823.18, obsd. 823.27.

2.2. UV–vis spectra

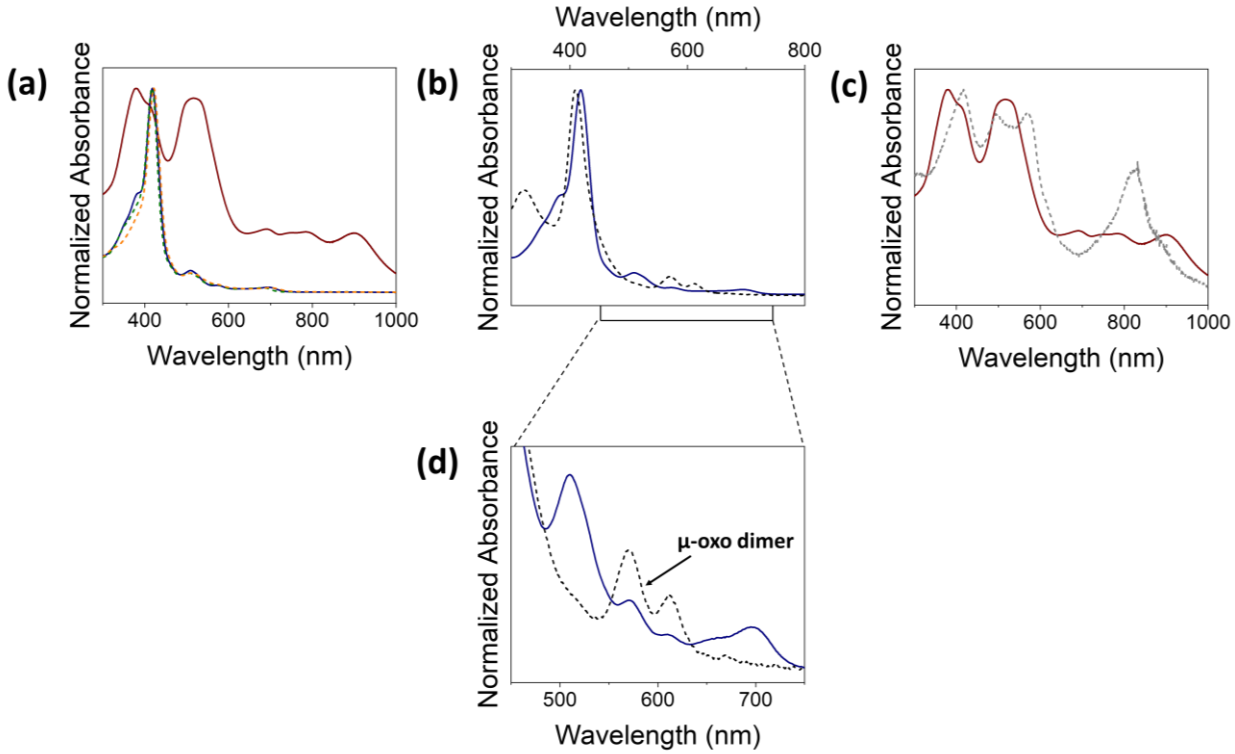

Figure S1. Normalized UV–vis absorption spectra recorded using *N*,*N'*-dimethylformamide solutions containing either [Fe_2FP]Cl_2 (0.13 mM) (red solid), [FeTTP]Cl (0.13 mM) (blue solid), [FeT*p*CF_3PP]Cl (0.13 mM) (green dash), or [FeT*p*OMePP]Cl (0.13 mM) (orange dash). The relatively red absorption features associated with [Fe_2FP]Cl_2 versus [FeTTP]Cl, [FeT*p*CF_3PP]Cl, and [FeT*p*OMePP]Cl are consistent with the π-extended conjugation (*i.e.*, the interaction of one π-orbital with another across a system of alternating single and multiple bonds)[10] of the fused architecture.[11] Although multinuclear fused porphyrins have been fairly well studied due in part to the unique optical properties,[12–14] they have not been as extensively studied for applications in electrocatalysis.[3,15–17] (b) Normalized UV–vis absorption spectra recorded using *N*,*N'*-dimethylformamide solutions of [FeTTP]Cl diluted to 0.13 mM in porphyrin (blue solid) or 0.05 mM in porphyrin (black dash) (adapted with permission from Reyes Cruz *et al.*[3] Copyright 2021 John Wiley and Sons). The difference in the normalized electronic spectra recorded at the more concentrated versus dilute conditions are attributed to the formation of μ-oxo dimers at lower concentrations via reactions with residual water.[18] (c) Normalized UV–vis absorption spectra recorded using *N*,*N'*-dimethylformamide solutions of [Fe_2FP]Cl_2 diluted to 0.13 mM in porphyrin (red solid) or 3.9 μM in porphyrin (gray dash). Under these conditions—using *N*,*N'*-dimethylformamide solutions of the fused porphyrin complex, [Fe_2FP]Cl_2—differences are also observed in the normalized electronic spectra recorded at the more concentrated versus dilute conditions. (d) An expanded plot comparing normalized absorption spectra recorded using *N*,*N'*-dimethylformamide solutions of [FeTTP]Cl diluted to 0.25 mM in porphyrin (blue solid) (adapted with permission from Reyes Cruz *et al.*[3] Copyright 2021 John Wiley and Sons) or 0.05 mM in porphyrin (black dash) (adapted with permission from Reyes Cruz *et al.*[3] Copyright 2021 John Wiley and Sons) is included for facilitating comparisons of spectral features in the porphyrin Q-band region.

2.3. FTIR spectra

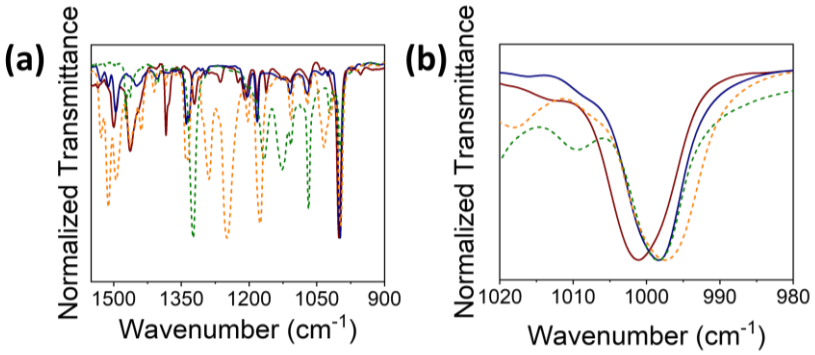

Figure S2. (a) Normalized FTIR transmission spectra collected using samples of $[Fe_2FP]Cl_2$ (red solid), [FeTTP]Cl (blue solid), [FeT*p*CF_3PP]Cl (green dash), or [FeT*p*OMePP]Cl (orange dash). (b) An expanded plot of the 980–1020 cm^{-1} region of the spectra shown in panel a. All spectra were recorded using KBr as a sample matrix. All spectra were recorded at 1 cm^{-1} resolution.

2.4. Mass spectra

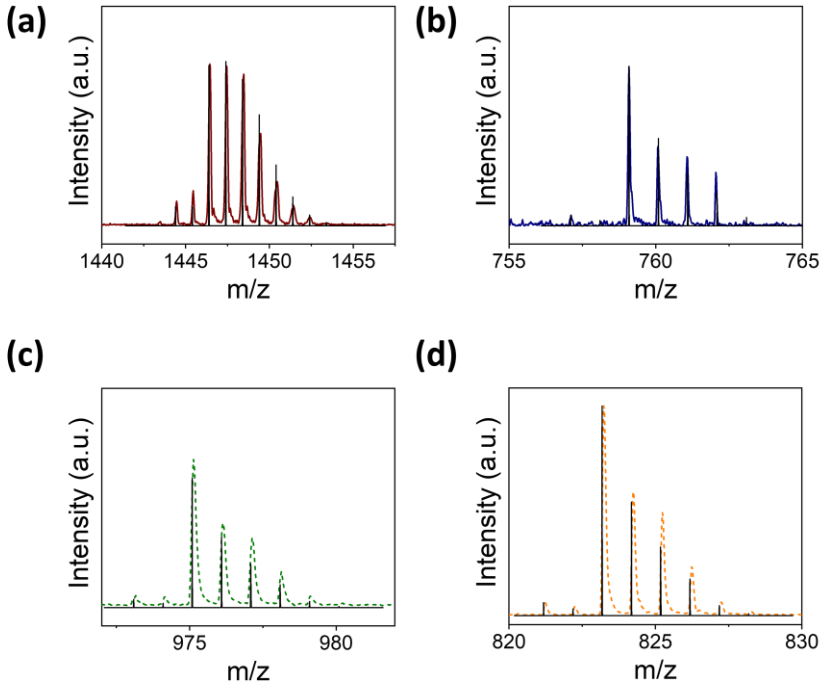

Figure S3. MALDI-TOF mass spectra collected using (a) $[Fe_2FP]Cl_2$ (red solid), (b) [FeTTP]Cl (blue solid), (c) [FeT*p*CF_3PP]Cl (green dash), or (d) [FeT*p*OMePP]Cl (orange dash). The calculated isotopic distribution for each compound (black) is included for comparison.

2.5. NMR spectra

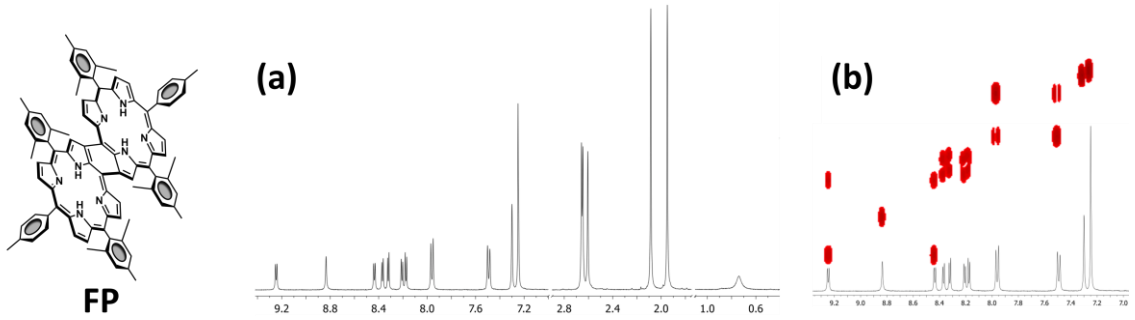

Figure S4. (a) ^{1}H NMR spectrum of *meso*-β doubly-fused 5,24-di-(*p*-tolyl)-10,19,29,38-tetramesitylporphyrin (FP) recorded in deuterochloroform and (b) the same spectrum (black) expanded to show the aromatic region with overlaid COSY data (red). The structure of FP is shown to the left.

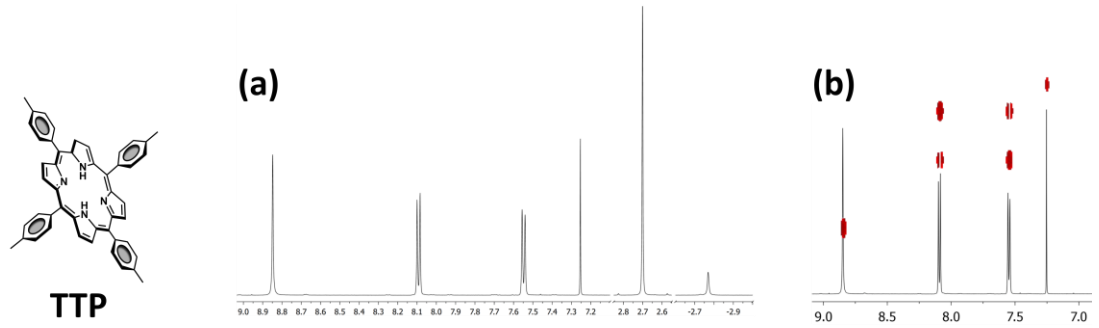

Figure S5. (a) ^{1}H NMR spectrum of 5,10,15,20-tetrakis(4-methylphenyl)porphyrin (TTP) recorded in deuterochloroform and (b) the same spectrum (black) expanded to show the aromatic region with overlaid COSY data (red). The structure of TTP is shown to the left.

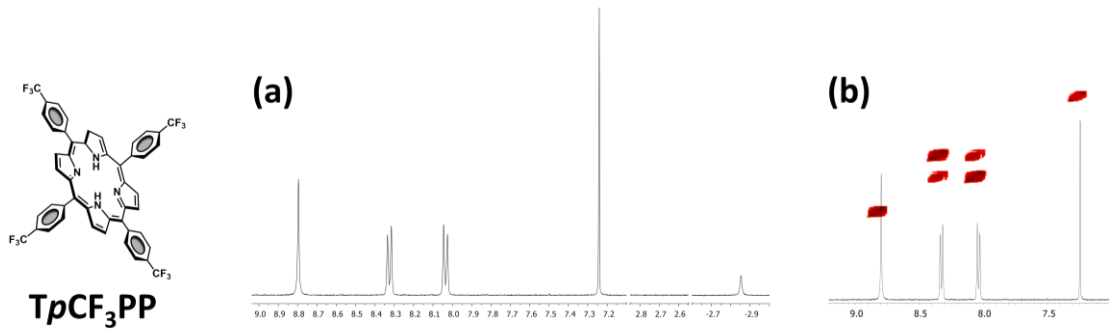

Figure S6. (a) ^{1}H NMR spectrum of 5,10,15,20-tetrakis[4-(trifluoromethyl)phenyl]porphyrin (T*p*CF_3PP) recorded in deuterochloroform and (b) the same spectrum (black) expanded to show the aromatic region with overlaid COSY data (red). The structure of T*p*CF_3PP is shown to the left.

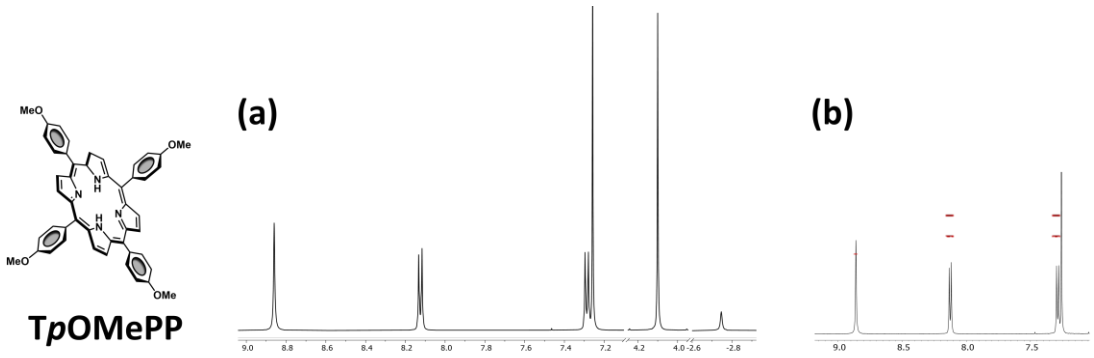

Figure S7. (a) ^{1}H NMR spectrum of 5,10,15,20-tetrakis(4-methoxyphenyl)porphyrin (T*p*OMePP) recorded in deuterochloroform and (b) the same spectrum (black) expanded to show the aromatic region with overlaid COSY data (red). The structure of T*p*OMePP is shown to the left.

2.6. Voltammetry data

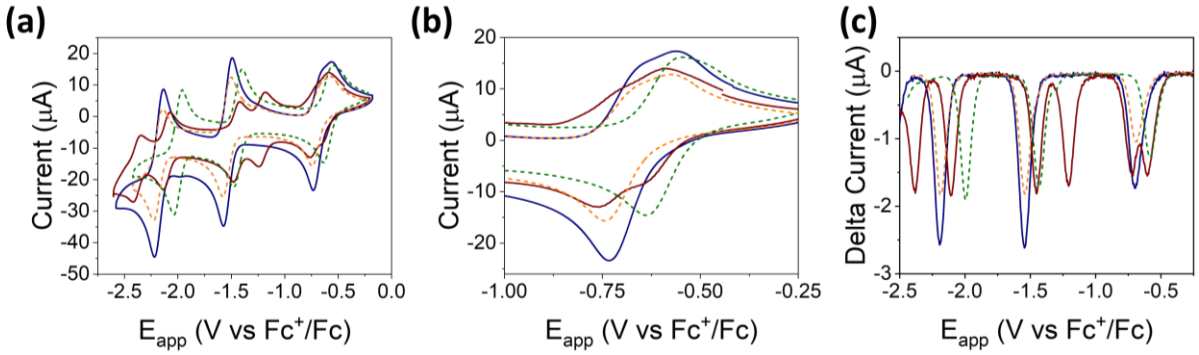

Figure S8. (a) Cyclic voltammograms recorded under argon (1 atm) using *N,N'*-dimethylformamide solutions containing $[Fe_2FP]Cl_2$ (1 mM) (red solid), [FeTTP]Cl (1 mM) (blue solid), [FeT*p*CF_3PP]Cl (1 mM) (green dash), or [FeT*p*OMePP]Cl (1 mM) (orange dash). All data were recorded at a scan rate of 250 mV s^{-1} and using solutions containing $TBAPF_6$ (0.1 M) as a supporting electrolyte. (b) An expanded plot of the data shown in panel a and showing the corresponding $Fe^{III/II}$ redox couples (*i.e.*, $[Fe_2FP]^{2+}/[Fe_2FP]^{1+}$, $[Fe_2FP]^{1+}/[Fe_2FP]^{0}$, $[FeTTP]^{1+}/[FeTTP]^{0}$, $[FeTpCF_3PP]^{1+}/[FeTpCF_3PP]^{0}$, or $[FeTpOMePP]^{1+}/[FeTpOMePP]^{0}$ couple). (c) Differential pulse voltammetry data of the same solutions recorded with a pulse height of 2.5 mV, a pulse width of 100 ms, a step height of –5 mV, and a step time of 500 ms. Although the redox processes are indicated as metal-centered, differentiating metal-centered versus ligand-based redox processes can be challenging and redox processes involving metalloporphyrins have been ascribed to both innocent and non-innocent (*i.e.*, guilty) ligand chemistry.[19–25]

2.7. XP spectra and XANE spectra

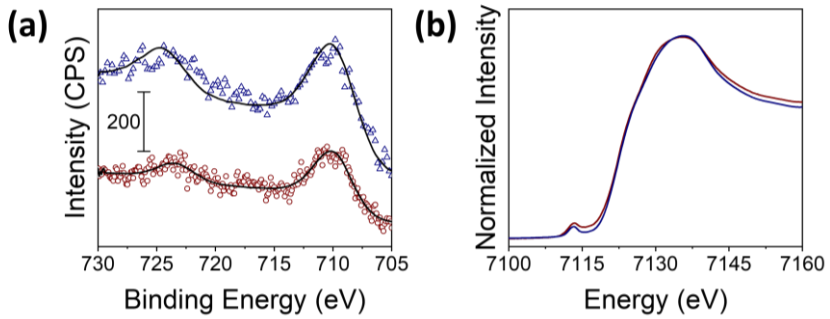

Figure S9. (a) High energy resolution Fe 2p core level X-ray photoelectron (XP) spectra region recorded using samples of $[Fe_2FP]_2$ (red) or [FeTTP]Cl (blue) prepared via dropcasting onto a glassy carbon disk using dichloromethane as a solvent. The solid black lines are the component fits. (b) Fe K-edge X-ray absorption near-edge (XANE) spectra recorded using samples of $[Fe_2FP]_2$ (red) or [FeTTP]Cl (blue) dropcasted onto a glassy carbon disk. Adapted with permission from Reyes Cruz *et al.*[3] Copyright 2021 John Wiley and Sons.

3. MicroED data

Table S1. MicroED data collection and refinement statistics.

	[Fe_2FP]Cl_2
Data collection	
Excitation Voltage	300 kV
Wavelength (Å)	0.019687
Number of crystals	4
Data Processing	
Space group	C2/c
Unit cell length a, b, c (Å)	36.30, 9.94, 23.29
Angles α, β, ɣ (°)	90.000, 115.066, 90.000
Resolution (Å)	0.80
Number of reflections	30,758
Unique reflections	7,607
R_{obs} (%)	12.4 (104.5)
R_{meas} (%)	12.1 (69.6)
I/σ_I	5.50 (0.48)
$CC_{1/2}$ (%)	99.6 (31.3)
Completeness (%)	91.8 (34.2)
Structure Refinement	
R1	0.2032 (0.1562 $F_o > 4\sigma$)
wR2	0.4567
GooF	1.514

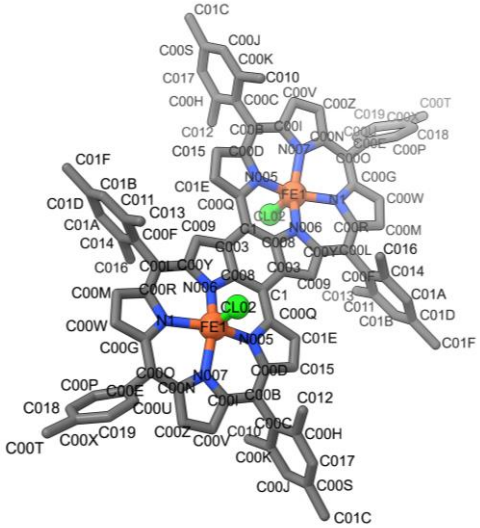

Figure S10. Molecular structure of [Fe_2FP]Cl_2 with atomic numbering. Hydrogen atoms are omitted for clarity.

Table S2. Bond lengths.

Atom	Atom	Length (Å)	Atom	Atom	Length (Å)
C003	C008	1.49(1)	C00W	H00W	0.929
C003	C009	1.39(1)	C00X	C018	1.38(1)
C008	C1	1.42(1)	C00X	C019	1.41(1)
C009	H009	0.931	C00Z	H00Z	0.931
C009	C00Y	1.424(9)	C010	H01A	0.96
C00B	C00C	1.51(1)	C010	H01B	0.96
C00B	C00D	1.43(1)	C010	H01C	0.96
C00B	C00I	1.44(1)	C011	C013	1.56(1)
C00C	C00H	1.39(1)	C011	C01B	1.41(2)
C00C	C00K	1.47(1)	C012	H01D	0.959
C00D	C015	1.48(1)	C012	H01E	0.96
C00E	C00O	1.52(1)	C012	H01F	0.96
C00E	C00P	1.44(1)	C013	H01G	0.96
C00E	C00U	1.42(1)	C013	H01H	0.96
C00F	C00L	1.52(1)	C013	H01I	0.96
C00F	C011	1.41(1)	C014	C016	1.50(2)
C00F	C014	1.42(1)	C014	C01A	1.43(1)
C00G	C00O	1.41(1)	C015	H015	0.93
C00G	C00W	1.45(1)	C015	C01E	1.35(1)
C00G	N1	1.399(9)	C016	H01J	0.96
C00H	C012	1.52(1)	C016	H01K	0.96
C00H	C017	1.44(1)	C016	H01L	0.961
C00I	C00V	1.44(1)	C017	H017	0.93
C00J	H00J	0.93	C018	H018	0.931
C00J	C00K	1.40(1)	C019	H019	0.93
C00J	C00S	1.42(1)	C01A	H01M	0.93
C00K	C010	1.52(1)	C01A	C01D	1.42(2)
C00L	C00R	1.42(1)	C01B	H01N	0.93
C00L	C00Y	1.45(1)	C01B	C01D	1.43(2)
C00M	H00M	0.93	C01C	H01O	0.96
C00M	C00R	1.45(1)	C01C	H01P	0.96
C00M	C00W	1.40(1)	C01C	H01Q	0.96
C00N	C00O	1.44(1)	C01D	C01F	1.52(2)
C00N	C00Z	1.45(1)	C01E	H01R	0.93
C00P	H00P	0.93	C01F	H01S	0.96
C00P	C018	1.39(1)	C01F	H01T	0.96
C00Q	C1	1.48(1)	C01F	H01U	0.96

C00Q	C01E	1.42(2)	Cl02	Fe1	2.247(5)
C00R	N1	1.42(1)	Fe1	N1	2.125(7)
C00S	C017	1.42(1)	N005	C00D	1.38(1)
C00S	C01C	1.51(2)	N005	C00Q	1.403(9)
C00T	H00A	0.96	N005	Fe1	2.124(8)
C00T	H00B	0.959	N006	C008	1.394(9)
C00T	H00C	0.96	N006	C00Y	1.40(1)
C00T	C00X	1.54(1)	N006	Fe1	2.117(6)
C00U	H00U	0.93	N007	C00I	1.39(1)
C00U	C019	1.41(1)	N007	C00N	1.408(9)
C00V	H00V	0.93	N007	Fe1	2.137(7)
C00V	C00Z	1.38(1)			

Table S3. Bond angles.

Atom	Atom	Atom	Angle (°)	Atom	Atom	Atom	Angle (°)
C003	C008	N006	110.7(6)	C00N	C00Z	C00V	106.9(7)
C003	C008	C1	122.0(6)	C00N	N007	Fe1	127.0(5)
C003	C009	C00Y	109.4(6)	C00N	C00Z	C00V	106.9(7)
C003	C008	N006	110.7(6)	C00O	C00E	C00P	121.9(7)
C003	C008	C1	122.0(6)	C00O	C00E	C00U	121.5(7)
C003	C009	C00Y	109.4(6)	C00O	C00G	C00W	123.3(7)
C003	C1	C008	115.4(6)	C00O	C00G	N1	125.1(7)
C003	C1	C00Q	122.1(6)	C00O	C00N	C00Z	124.6(7)
C008	C003	C009	103.9(6)	C00O	C00E	C00P	121.9(7)
C008	C003	C1	122.6(6)	C00O	C00E	C00U	121.5(7)
C008	N006	C00Y	105.7(6)	C00O	C00G	C00W	123.3(7)
C008	N006	Fe1	126.7(5)	C00O	C00G	N1	125.1(7)
C008	C1	C00Q	122.3(6)	C00O	C00N	C00Z	124.6(7)
C008	C1	C003	115.4(6)	C00P	C00E	C00U	116.1(7)
C008	C003	C009	103.9(6)	C00P	C018	C00X	124.3(9)
C008	N006	C00Y	105.7(6)	C00P	C00E	C00U	116.1(7)
C008	N006	Fe1	126.7(5)	C00P	C018	C00X	124.3(9)
C008	C1	C00Q	122.3(6)	C00Q	N005	Fe1	128.4(5)
C009	C003	C1	133.5(6)	C00Q	C1	C003	122.1(6)
C009	C00Y	C00L	123.4(7)	C00Q	C01E	C015	108.1(9)
C009	C00Y	C00L	123.4(7)	C00Q	N005	Fe1	128.4(5)
C00B	C00C	C00H	120.1(7)	C00Q	C01E	C015	108.1(9)
C00B	C00C	C00K	118.6(7)	C00R	C00L	C00Y	123.8(7)
C00B	C00D	C015	122.6(8)	C00R	C00M	C00W	107.8(7)

C00B	C00I	C00V	124.0(7)	C00R	N1	Fe1	125.1(5)
C00B	C00C	C00H	120.1(7)	C00R	C00L	C00Y	123.8(7)
C00B	C00C	C00K	118.6(7)	C00R	C00M	C00W	107.8(7)
C00B	C00D	C015	122.6(8)	C00R	N1	Fe1	125.1(5)
C00B	C00I	C00V	124.0(7)	C00T	C00X	C018	122.6(8)
C00C	C00B	C00D	121.3(7)	C00T	C00X	C019	121.2(7)
C00C	C00B	C00I	115.8(7)	C00T	C00X	C018	122.6(8)
C00C	C00H	C012	122.6(7)	C00T	C00X	C019	121.2(7)
C00C	C00H	C017	119.2(7)	C00U	C019	C00X	121.8(8)
C00C	C00K	C00J	116.4(8)	C00U	C019	C00X	121.8(8)
C00C	C00K	C010	122.0(8)	C00W	C00G	N1	111.1(7)
C00C	C00B	C00D	121.3(7)	C00W	C00G	N1	111.1(7)
C00C	C00B	C00I	115.8(7)	C00Y	N006	Fe1	125.8(5)
C00C	C00H	C012	122.6(7)	C00Y	N006	Fe1	125.8(5)
C00C	C00H	C017	119.2(7)	C011	C00F	C014	121.0(8)
C00C	C00K	C00J	116.4(8)	C011	C01B	C01D	122(1)
C00C	C00K	C010	122.0(8)	C011	C00F	C014	121.0(8)
C00D	N005	C00Q	107.0(6)	C011	C01B	C01D	122(1)
C00D	N005	Fe1	123.6(5)	C012	C00H	C017	118.2(7)
C00D	C00B	C00I	122.9(7)	C012	C00H	C017	118.2(7)
C00D	C015	C01E	107.6(9)	C013	C011	C01B	118.5(9)
C00D	N005	C00Q	107.0(6)	C013	C011	C01B	118.5(9)
C00D	N005	Fe1	123.6(5)	C014	C01A	C01D	121.7(9)
C00D	C00B	C00I	122.9(7)	C014	C01A	C01D	121.7(9)
C00D	C015	C01E	107.6(9)	C016	C014	C01A	118.3(8)
C00E	C00O	C00G	120.5(7)	C016	C014	C01A	118.3(8)
C00E	C00O	C00N	116.6(7)	C017	C00S	C01C	121.3(9)
C00E	C00P	C018	120.1(8)	C017	C00S	C01C	121.3(9)
C00E	C00U	C019	121.2(7)	C018	C00X	C019	116.2(8)
C00E	C00O	C00G	120.5(7)	C018	C00X	C019	116.2(8)
C00E	C00O	C00N	116.6(7)	C01A	C01D	C01B	117(1)
C00E	C00P	C018	120.1(8)	C01A	C01D	C01F	122(1)
C00E	C00U	C019	121.2(7)	C01A	C01D	C01B	117(1)
C00F	C00L	C00R	119.3(7)	C01A	C01D	C01F	122(1)
C00F	C00L	C00Y	116.9(7)	C01B	C01D	C01F	121(1)
C00F	C011	C013	121.9(8)	C01B	C01D	C01F	121(1)
C00F	C011	C01B	119.6(9)	C1	C00Q	C01E	126.5(8)
C00F	C014	C016	123.2(8)	C1	C003	C008	122.6(6)
C00F	C014	C01A	118.4(8)	C1	C003	C009	133.5(6)
C00F	C00L	C00R	119.3(7)	C1	C00Q	C01E	126.5(8)
C00F	C00L	C00Y	116.9(7)	Cl02	Fe1	N005	102.5(2)

C00F	C011	C013	121.9(8)	Cl02	Fe1	N006	103.6(2)
C00F	C011	C01B	119.6(9)	Cl02	Fe1	N007	105.7(2)
C00F	C014	C016	123.2(8)	Cl02	Fe1	N1	104.0(2)
C00F	C014	C01A	118.4(8)	N005	C00D	C00B	129.5(7)
C00G	C00O	C00N	122.7(7)	N005	C00D	C015	107.7(7)
C00G	C00W	C00M	106.0(7)	N005	C00Q	C1	124.0(7)
C00G	N1	C00R	105.7(6)	N005	C00Q	C01E	109.6(8)
C00G	N1	Fe1	127.1(5)	N005	Fe1	N006	85.6(3)
C00G	C00O	C00N	122.7(7)	N005	Fe1	N007	88.2(3)
C00G	C00W	C00M	106.0(7)	N005	Fe1	N1	153.6(3)
C00G	N1	C00R	105.7(6)	N005	C00D	C00B	129.5(7)
C00G	N1	Fe1	127.1(5)	N005	C00D	C015	107.7(7)
C00H	C00C	C00K	121.2(7)	N005	C00Q	C1	124.0(7)
C00H	C017	C00S	121.5(8)	N005	C00Q	C01E	109.6(8)
C00H	C00C	C00K	121.2(7)	N005	Fe1	N006	85.6(3)
C00H	C017	C00S	121.5(8)	N005	Fe1	N007	88.2(3)
C00I	N007	C00N	106.3(6)	N005	Fe1	N1	153.6(3)
C00I	N007	Fe1	126.3(5)	N005	Fe1	Cl02	102.5(2)
C00I	C00V	C00Z	107.5(7)	N006	C008	C1	127.3(6)
C00I	N007	C00N	106.3(6)	N006	C00Y	C009	110.2(6)
C00I	N007	Fe1	126.3(5)	N006	C00Y	C00L	126.3(7)
C00I	C00V	C00Z	107.5(7)	N006	Fe1	N007	150.7(3)
C00J	C00K	C010	121.6(8)	N006	Fe1	N1	88.3(3)
C00J	C00S	C017	117.0(9)	N006	C008	C1	127.3(6)
C00J	C00S	C01C	121.8(9)	N006	C00Y	C009	110.2(6)
C00J	C00K	C010	121.6(8)	N006	C00Y	C00L	126.3(7)
C00J	C00S	C017	117.0(9)	N006	Fe1	N007	150.7(3)
C00J	C00S	C01C	121.8(9)	N006	Fe1	N1	88.3(3)
C00K	C00J	C00S	124.7(9)	N006	Fe1	Cl02	103.6(2)
C00K	C00J	C00S	124.7(9)	N007	C00I	C00B	125.9(7)
C00L	C00F	C011	121.3(7)	N007	C00I	C00V	109.9(7)
C00L	C00F	C014	117.6(7)	N007	C00N	C00O	126.2(7)
C00L	C00R	C00M	123.7(7)	N007	C00N	C00Z	109.2(7)
C00L	C00R	N1	127.0(7)	N007	Fe1	N1	84.6(3)
C00L	C00F	C011	121.3(7)	N007	C00I	C00B	125.9(7)
C00L	C00F	C014	117.6(7)	N007	C00I	C00V	109.9(7)
C00L	C00R	C00M	123.7(7)	N007	C00N	C00O	126.2(7)
C00L	C00R	N1	127.0(7)	N007	C00N	C00Z	109.2(7)
C00M	C00R	N1	109.3(7)	N007	Fe1	N1	84.6(3)
C00M	C00R	N1	109.3(7)	N007	Fe1	Cl02	105.7(2)
C00N	N007	Fe1	127.0(5)	N1	Fe1	Cl02	104.0(2)

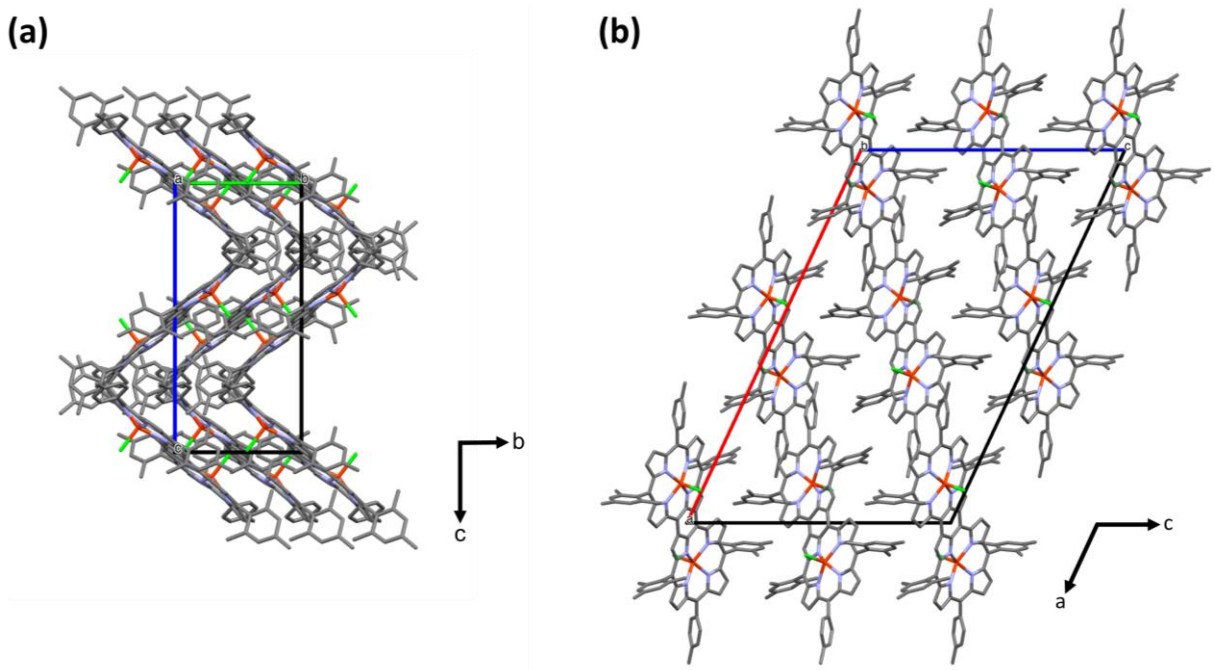

Figure S11. Packing in the crystalline state of $[Fe_2FP]Cl_2$ viewed along the (a) a-axis and (b) b-axis.

4. Computational analysis

To establish the most likely spin state in these relatively large molecular assemblies, a combination of 'Geometries, Frequencies, Noncovalent interactions extended Tight Binding' (GFN-xTB), and density functional theory (DFT)—that was previously shown to give good results with low computational cost—was used. Molecules were optimized with GFN-xTB, including a frequency analysis for Gibbs free energy correction terms in vacuum, before using these optimized structures as input for DFT geometry optimizations using implicit *N*,*N'*-dimethylformamide solvent. For this, a reduced system was used to prevent convergence issues by removing *para*-substituted methyl groups on the phenyl rings, as the low rotation barrier poses convergence issues. The model is shown in Figure S12.

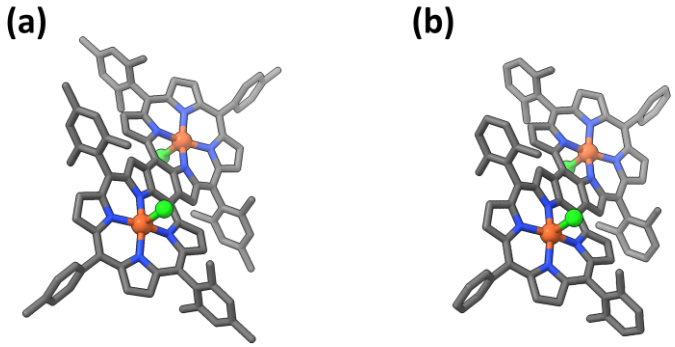

Figure S12. (a) Full molecular model and (b) slightly simplified model for improved convergence. Hydrogens are omitted for clarity.

Different spin states were tested, with partial occupations in GFN-xTB (with no Fermi smearing) and full unrestricted optimizations following wave function stability check for the DFT simulations. Electronic energies were extracted from the DFT results, with Gibbs free energy corrections (G correction) extracted from GFN-xTB frequency analysis. Energies, Gibbs free energy corrections, and Gibbs free energies of molecules in different spin states and with different chloride orientations are collected in Table S4.

Table S4. Electronic energies determined by DFT optimization, Gibbs free energy correction (G correction) terms from GFN-xTB frequency analysis and combined Gibbs free energy obtained using the DFT+xTB method for spin states singlet to undecet in implicit *N,N'*-dimethylformamide solvent for both configurations of the $[Fe_2FP]Cl_2$ molecule. All values are given in eV. The lowest energy spin state for each configuration is marked in bold. The relative Gibbs free energy (relative G) is with regards to the lowest energy spin state and configuration: the *anti* configuration in the septet state.

***Anti* configuration**						
Spin state	**Singlet**	**Triplet**	**Quintet**	**Septet**	**Nonet**	**Undecet**
Electronic Energy	–193764.729	–193765.088	–193765.573	**–193766.600**	–193764.995	–193765.814
G Correction	+28.774	+28.780	+28.717	**+28.659**	+28.637	+28.557
Gibbs Free Energy	–193735.955	–193736.308	–193736.857	**–193737.942**	–193736.358	–193737.257
Relative G	+1.987	+1.634	+1.085	**0.000**	+1.584	+0.685
***Syn* configuration**						
Spin state	**Singlet**	**Triplet**	**Quintet**	**Septet**	**Nonet**	**Undecet**
Electronic Energy	–193764.758	–193764.966	–193766.062	**–193766.542**	–1937365.539	–193765.407
G Correction	+28.782	+28.777	+28.730	**+28.673**	+28.646	+28.551
Gibbs Free Energy	–193735.976	–193736.189	–193737.332	**–193737.869**	–193736.893	–193736.856
Relative G	+1.966	+1.753	+0.610	**+0.073**	+1.049	+1.086

For the *anti* configuration, a DFT optimization of the full system was also computed to compare the results to the crystal structure (see main text and Figure S13) and for orbital and spin structure investigations. The conformation optimized from the crystal structure has a higher energy than the conformation obtained from GFN-xTB starting structure. The energy and dipole moment of these two conformations are given in Table S5.

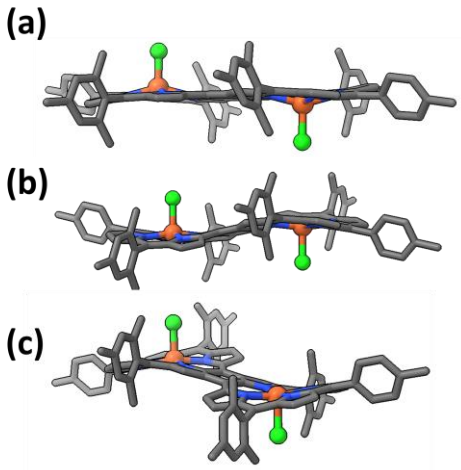

Figure S13. Structures of $[Fe_2FP]Cl_2$ determined by (a) MicroED, (b) DFT optimization starting from the crystal structure, and (c) DFT optimization starting from a GFN-xTB geometry.

The structures of porphyrins, including ring bending, are highly dependent on environmental factors,[26] and the different geometries of $[Fe_2FP]Cl_2$ in the solid versus solution phases indicated via our computational analysis might arise from distinctions associated with the environments of these phases. In the crystalline form, the more ordered structure favors well-defined molecular orientations. Conversely, the more disordered environment in solution results in the cancellation of directional, anisotropic interactions. Polar solvents are known to stabilize molecular dipole moments due to their ability to rearrange around the solute and the favorability of the dipole-dipole interactions,[27] including in porphyrins. One further example is the effect solvents of different polarity have on the excited state and spectroscopic properties of porphyrins, where for example, excited states with high charge transfer character are stabilized in polar solvents.[28] The lower energy conformer optimized with DFT from an GFN-xTB based geometry has a higher molecular dipole moment than the conformer derived from the crystal structure (see Table S5). This is attributed to the solvent stabilization of the dipole moment and is consistent with the relative stability of this conformer in the solution phase. However, the difference in energy between these conformers (Δ = 97 meV) is relatively small and within the intrinsic approximations of DFT and implicit solvent models.

Table S5. Electronic energies and dipole moments determined by DFT geometry optimizations, for both conformations of the $[Fe_2FP]Cl_2$ molecule in implicit *N,N'*-dimethylformamide. Conformation 1 is obtained starting from the crystal structure geometry, while conformation 2 was obtained when starting the DFT optimization from a GFN-xTB geometry.

Conformation	Starting geometry obtained by	Electronic Energy (eV)	Dipole moment (Debye)
1 (see Figure S13b)	Crystal structure	–200181.109	0.0002
2 (see Figure S13c)	GFN-xTB	–200181.206	0.1597
Difference		–0.097	

In comparison, Table S6 shows the electronic energy, Gibbs free energy corrections, and Gibbs free energy of different spin states of the [FeTTP]Cl complex. Figure S14 shows a ligand field splitting scheme for the lowest Gibbs free energy spin states quartet and sextet, with key orbitals given. Note that the π* remains higher in energy than the d-orbitals of the iron center.

Table S6. Electronic energies of the [FeTTP]Cl in different spin states and relative energies normalized on the quartet state in eV obtained by DFT geometry optimization, as well as the Gibbs free energy correction terms obtained by GFN-xTB and the corresponding Gibbs free energy obtained using the DFT+xTB method in eV. The lowest column gives the relative Gibbs free energy normalized on the quartet spin state.

Spin state	**Doublet**	**Quartet**	**Sextet**
Electronic Energy	–103197.901	–103198.395	–103198.345
G Correction	+18.913	+18.892	+18.846
Gibbs Free Energy	–103178.988	–103179.504	–103179.499
Relative G	+0.515	0.000	+0.005

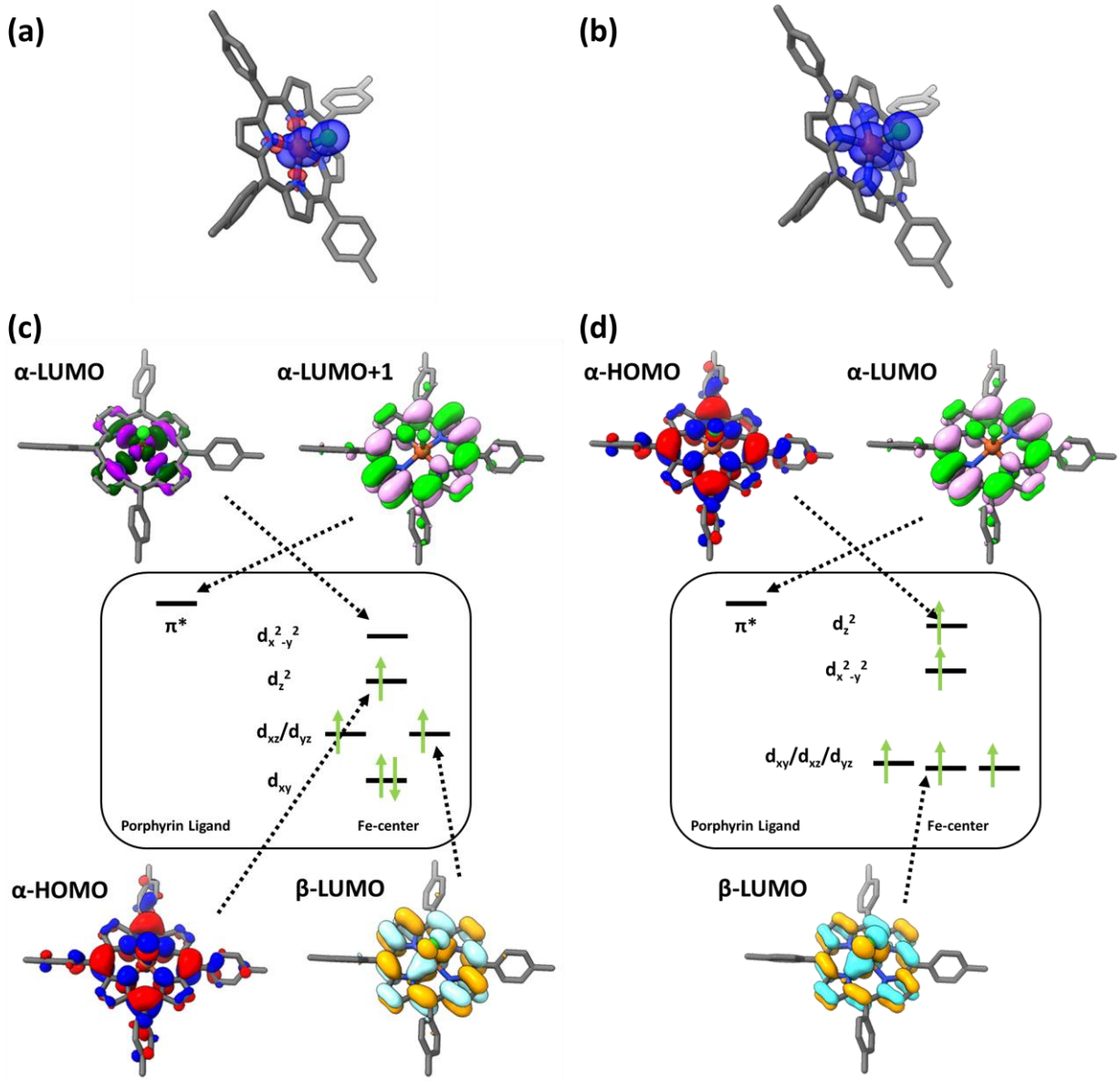

Figure S14. (a) and (b) DFT geometry overlaid with the spin density as shown in blue on the [FeTTP]Cl complex for the quartet (panel a) and sextet (panel b) spin states. (c) and (d) Molecular orbitals of the [FeTTP]Cl complex, showing contributions of specific d-orbitals for quartet (panel c) and sextet (panel d) spin states. In the inset, a schematic of the simplified ligand field splitting is given in comparison.

5. Electrochemical methods and additional voltammetry data

5.1. Acid concentration dependence

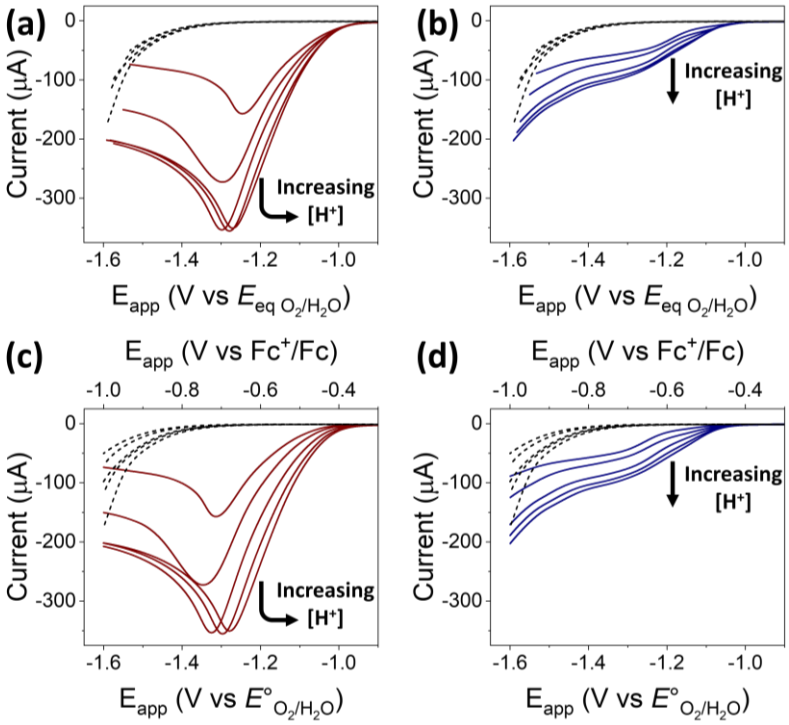

Figure S15. (a–d) Voltammograms recorded under O_2 (1 atm) using *N,N'*-dimethylformamide solutions containing increasing amounts of [$DMFH^+$][OTf^-] as a proton source (10, 20, 50, 70, and 100 mM) and either [Fe_2FP]Cl_2 (0.30 mM) (panels a and c, red) or [FeTTP]Cl (0.30 mM) (panels b and d, blue) as a catalyst. Voltammograms recorded in the absence of a catalyst (black dash) are included for comparison. All data were recorded at a scan rate of 100 mV s^{-1} using solutions containing $TBAPF_6$ (0.1 M) as a supporting electrolyte. In panels a and b, the applied electrode potentials are reported versus the equilibrium potential for the oxygen reduction half-reaction to form water ($E_{\mathrm{eq}\,O_2/H_2O}$) obtained using eq 5. The voltammograms displayed in panels a and b are the same as those in Figures 4a and 4b, but the extended x-axes show data collected at further cathodic polarization where uncatalyzed O_2 reduction at glassy carbon electrodes can contribute current. In panels c and d, the applied electrode potentials are reported versus either the ferrocenium/ferrocene redox couple (top abscissa) or the standard potential for the oxygen reduction half-reaction to form water ($E^0_{O_2/H_2O}$) (bottom abscissa), which is +0.60 V versus the ferrocenium/ferrocene redox couple.[29,30]

5.2. Rinse test

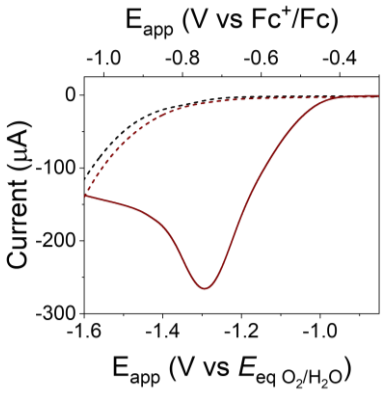

Figure S16. Voltammograms recorded prior to (red solid) and following (red dash) a *"rinse test,"* which is a method for detecting *in situ* formation of a heterogeneous or heterogenized active catalyst.[31–33] In these experiments, the voltammograms collected *"pre-rinse test"* were recorded under O_2 (1 atm) using *N,N'*-dimethylformamide solutions containing [$DMFH^+$][OTf^-] (20 mM) as a proton source, $TBAPF_6$ (0.1 M) as a supporting electrolyte, and [Fe_2FP]Cl_2 (0.30 mM) as a catalyst. The voltammograms collected *"post-rinse test"* were recorded after obtaining an initial voltammogram recorded under the pre-rinse test conditions, but after rinsing the working electrode with an *N,N'*-dimethylformamide solution containing $TBAPF_6$ (0.1 M) to remove any physisorbed species. The rinsed electrodes were moved to an electrochemical cell where the post-rinse test voltammetry measurements were performed under O_2 (1 atm) using *N,N'*-dimethylformamide solutions containing [$DMFH^+$][OTf^-] (20 mM) as a proton source, $TBAPF_6$ (0.1 M) as a supporting electrolyte, and no added catalyst. The lack of catalytic activity following the rinse test indicates there is minimal to no heterogenous, electrodeposited catalyst present on the electrode surfaces. A voltammogram recorded under O_2 (1 atm) using *N,N'*-dimethylformamide solutions containing [$DMFH^+$][OTf^-] (20 mM) as a proton source, $TBAPF_6$ (0.1 M) as a supporting electrolyte, a freshly polished glassy carbon disk as the working electrode, and no added catalyst (black dash) is included for comparison. All data were recorded at a scan rate of 100 mV s^{-1}.

5.3. Scan rate dependence

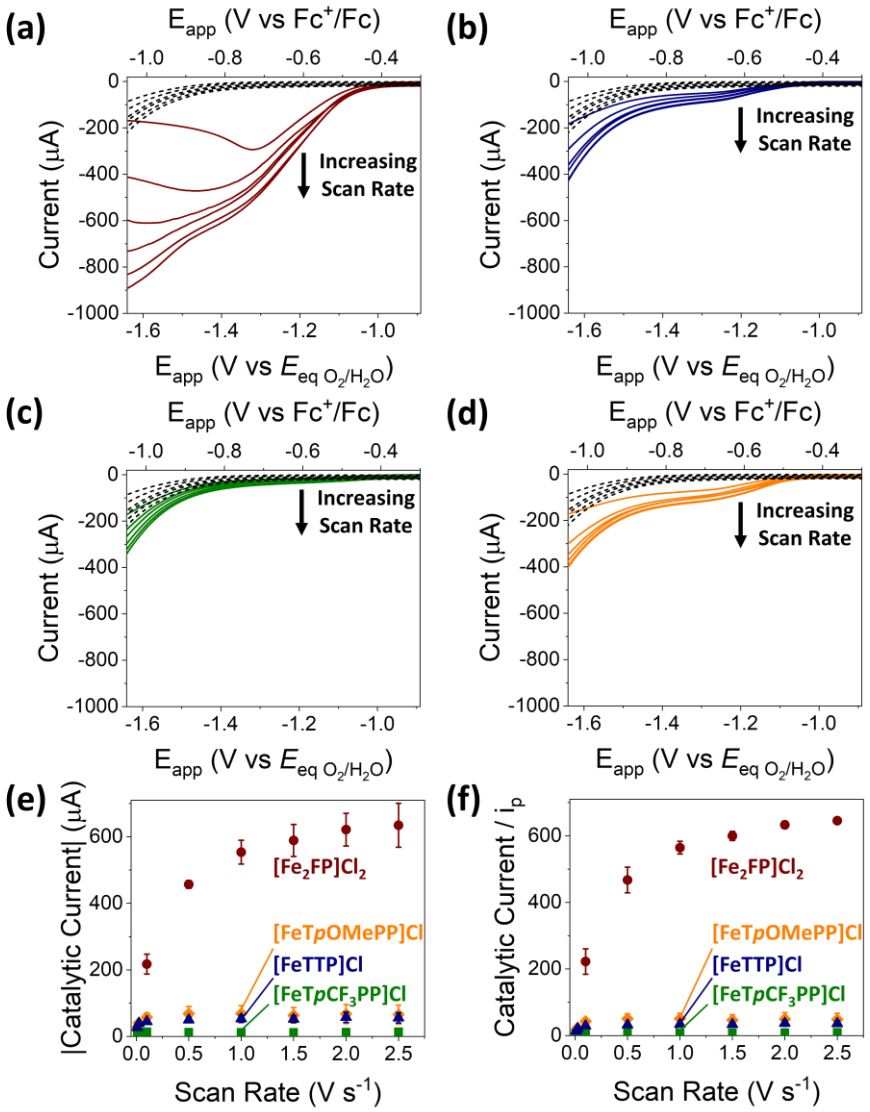

Figure S17. (a–d) Voltammograms recorded under O_2 (1 atm) and at increasing scan rates (100, 500, 1000, 1500, 2000, and 2500 mV s^{-1}) using *N,N'*-dimethylformamide solutions containing either $[Fe_2FP]Cl_2$ (0.14 mM) (panel a, red), [FeTTP]Cl (0.14 mM) (panel b, blue), [FeT*p*CF_3PP]Cl (0.14 mM) (panel c, green), or [FeT*p*OMePP]Cl (0.14 mM) (panel d, orange). Voltammograms recorded in the absence of a catalyst (black dash) are included for comparison. All solutions contained $[DMFH^+][OTf^-]$ (100 mM) as a proton source and $TBAPF_6$ (0.1 M) as a supporting electrolyte. (e) Catalytic current versus scan rate plots obtained from voltammetry measurements using either $[Fe_2FP]Cl_2$ (0.14 mM) (red circles), [FeTTP]Cl (0.14 mM) (blue triangles), [FeT*p*CF_3PP]Cl (0.14 mM) (green squares), or [FeT*p*OMePP]Cl (0.14 mM) (orange diamonds) as a catalyst. (f) Ratio of a catalytic current to peak current (i_p) versus scan rate plots obtained from voltammetry measurements using either $[Fe_2FP]Cl_2$ (0.14 mM) (red circles), [FeTTP]Cl (0.14 mM) (blue triangles), [FeT*p*CF_3PP]Cl (0.14 mM) (green squares), or [FeT*p*OMePP]Cl (0.14 mM) (orange diamonds) as a catalyst. The catalytic currents are reported at potentials determined via analyzing the first derivative of corresponding voltammograms to identify a local minimum (see Figures S20–S24). Error bars indicate standard deviations obtained from

triplicate measurements. At relatively low scan rates (*e.g.*, 100–1000 mV s^{-1}), voltammograms recorded using $[Fe_2FP]Cl_2$ display peak-shaped waveforms with no apparent contributions arising from the background currents recorded in the absence of an added catalyst (see black dash traces in panel a). These observations are consistent with conditions where the current becomes limited by the diffusion of O_2 and the concentration of O_2 at the electrode is thus relatively low. In other words, currents arising from the uncatalyzed O_2 reduction at the glassy carbon surface should be suppressed since the concentration of O_2 at the electrode surface would differ from its bulk value under these conditions and there would be little to no O_2 available at the electrode. Conversely, at relatively high scan rates (*e.g.*, 1500–2500 mV s^{-1}), voltammograms recorded using $[Fe_2FP]Cl_2$ display increasing cathodic currents as the applied electrode potential is swept negative of ~–1.5 V vs $E_{\mathrm{eq}\ O_2/H_2O}$. These observations are consistent with conditions where the currents are no longer limited by the diffusion of O_2. In this case, currents arising from the uncatalyzed O_2 reduction at the glassy carbon surface can contribute to the overall current since the concentration of O_2 at the electrode surface is approximately equal to its bulk value under S-wave or near-S-wave conditions.

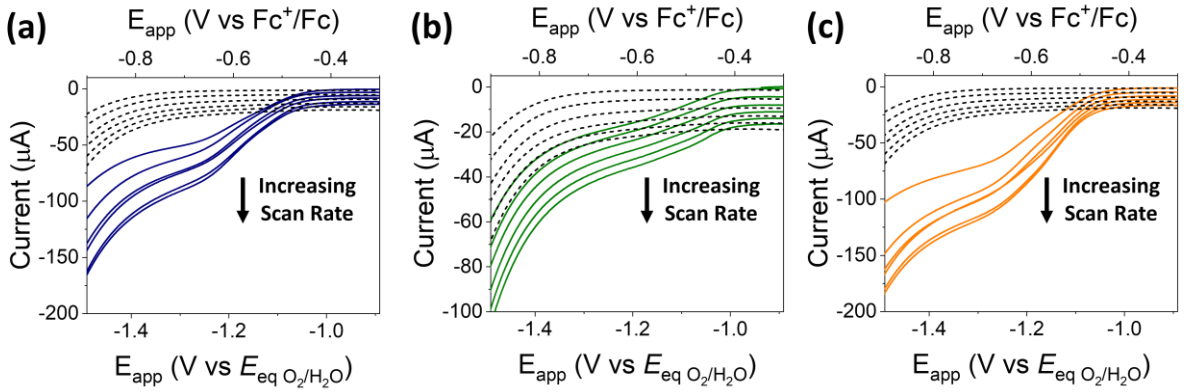

Figure S18. (a–c) Voltammograms showing a magnified scaling of the data presented in Figures S17b (recorded using [FeTTP]Cl), S17c (recorded using [FeT*p*CF_3PP]Cl), and S17d (recorded using [FeT*p*OMePP]Cl). These voltammograms were recorded under O_2 (1 atm) and at varying scan rates (100, 500, 1000, 1500, 2000, and 2500 mV s^{-1}) using *N,N'*-dimethylformamide solutions containing either [FeTTP]Cl (0.14 mM) (panel a, blue), [FeT*p*CF_3PP]Cl (0.14 mM) (panel b, green), or [FeT*p*OMePP]Cl (0.14 mM) (panel c, orange) as a catalyst. All solutions contained $[DMFH^+][OTf^-]$ (100 mM) as a proton source and $TBAPF_6$ (0.1 M) as a supporting electrolyte. Voltammograms recorded in the absence of a catalyst (black dash) are included for comparison.

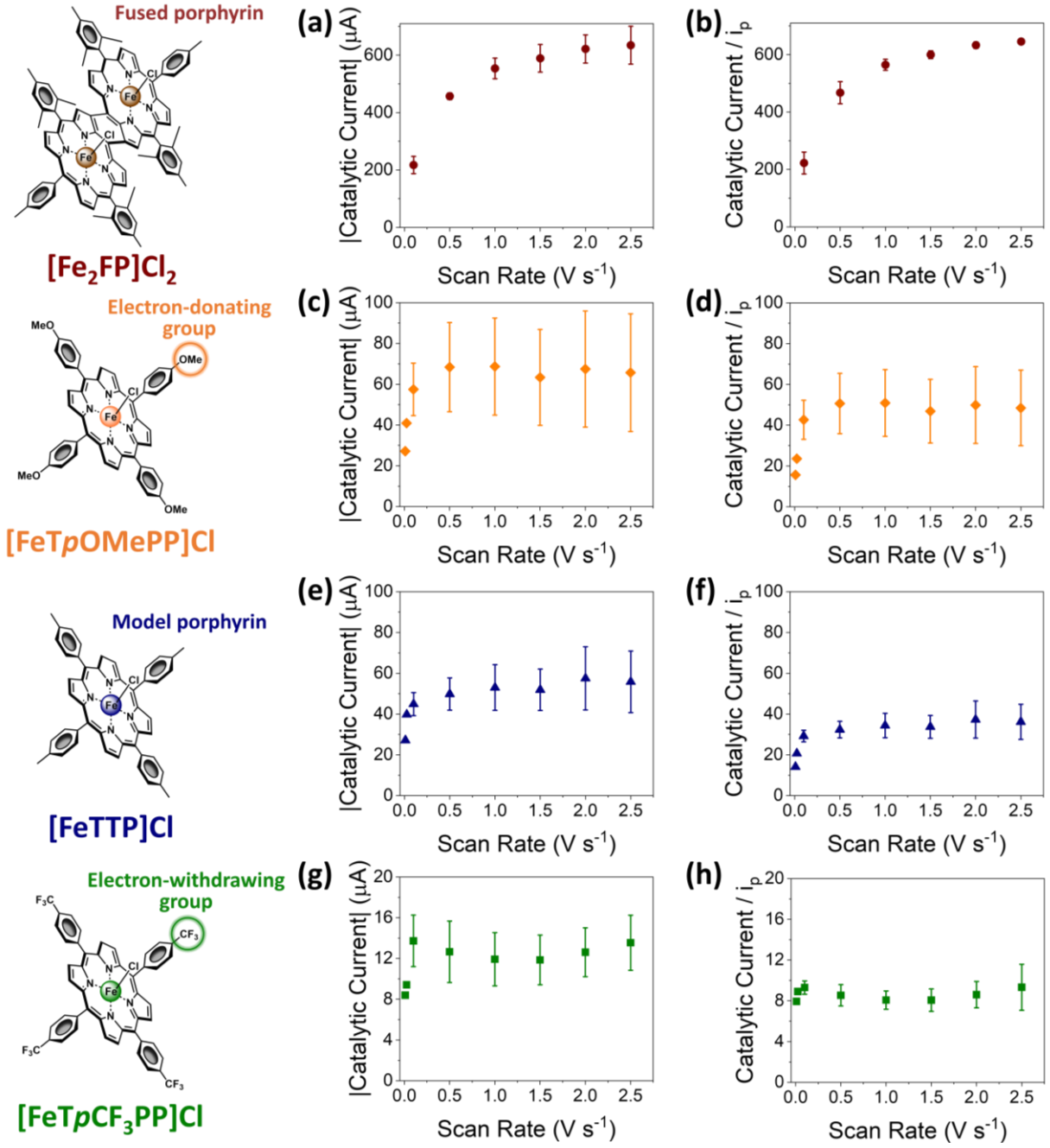

Figure S19. (a), (c), (e), and (g) Catalytic current versus scan rate plots obtained from voltammetry measurements using either $[Fe_2FP]Cl_2$ (0.14 mM) (panel a, red circles), [FeT*p*OMePP]Cl (0.14 mM) (panel c, orange diamonds), [FeTTP]Cl (0.14 mM) (panel e, blue triangles), or [FeT*p*CF_3PP]Cl (0.14 mM) (panel g, green squares) as a catalyst. (b), (d), (f), and (h) Ratio of catalytic current to the peak current (i_p) versus scan rate plots obtained from voltammetry measurements using either $[Fe_2FP]Cl_2$ (0.14 mM) (panel b, red circles), [FeT*p*OMePP]Cl (0.14 mM) (panel d, orange diamonds), [FeTTP]Cl (0.14 mM) (panel f, blue triangles), or [FeT*p*CF_3PP]Cl (0.14 mM) (panel h, green squares) as a catalyst. The catalytic currents are reported at potentials determined via analyzing the first derivative of corresponding voltammograms to identify a local minimum (see Figures S20–S24). Error bars indicate standard deviations obtained from triplicate measurements.

5.4. Determinations of maximum turnover frequencies, catalytic half-wave potentials, and catalytic plateau currents

The maximum turnover frequencies (TOF_{max} values) and catalytic half-wave potentials (**$E_{cat/2}$** values) reported in this work are obtained from triplicate sets of measurements performed using each catalyst and varying scan rate (meaning, three sets of voltammetry measurements were performed at scan rates ranging from 100 to 2500 mV s^{-1} for each of the four catalysts indicated in Chart S1) (see Figures 5a, 5b, S17a–17d, and S18). To account for contributions to the overall measured currents from charging currents (which increase with increasing scan rate), plots of catalytic current (see eq 11 in the main text of this article) versus scan rate were generated using each voltammogram recorded in the presence of an added catalyst via subtracting out the currents recorded in the absence of an added catalyst (see Figures S21–S24). Although this subtraction is useful to account for contributions from charging currents (and in part contributions attributed in our work and others to uncatalyzed oxygen reduction at a glassy carbon electrode surface under applied electrode potentials more negative than ~–1.6 V vs $E_{\mathrm{eq}\ O_2/H_2O}$),[34,35] the prevalence of a cathodic feature at applied electrode potentials more negative than ~–1.6 V vs $E_{\mathrm{eq}\ O_2/H_2O}$ contributes to deviations from an ideal S-shaped waveform. Therefore, a current within the plateau-shaped region of a voltammogram response—where the first derivative of the catalytic current yields a local minimum—was selected to (1) report the corresponding catalytic plateau current (i_{pl} value) and (2) identify a potential for reporting the values of catalytic currents in plots of catalytic current versus scan rate (see Figure S20). The reported values of i_{pl} are thus representative of the limiting catalytic currents that are approached in plots of catalytic current versus scan rate (*i.e.*, the values of catalytic current observed at conditions where the catalytic current is scan rate-independent).[36,37] The TOF_{max} values are in turn obtained from triplicate measurements of i_{pl} for each catalyst using eq 8 in the main text of this article. Further, each individual i_{pl} value contributing to a reported average and standard deviation was obtained from one set of experimental data recorded at varying scan rates, and the scan rate that yielded the highest catalytic current within that set was taken as representative (see Figures 5c, S17e, S17f, S19, and S21–S24). The corresponding values of $E_{cat/2}$ were determined from triplicate measurements of the half-wave potentials recorded using the same representative plots of catalytic current versus applied electrode potential used to determine the individual i_{pl} values and TOF_{max} values (see Figures S21–S24). The mean ($\bar{x}$) and sample standard deviation (*s*; also known as estimated standard deviation) values reported in this article were obtained using eqs S1 and S2,[10,38]

$$\bar{x} = \frac{\sum x_i}{n} \tag{S1}$$

$$s = \sqrt{\sum \frac{(x_i - \bar{x})^2}{n-1}} \tag{S2}$$

where n is the total number of measurements (in this article, n = 3), and x_i is the observed value in the i_{th} measurement of n total measurements (in this article, i = 1, 2, or 3).

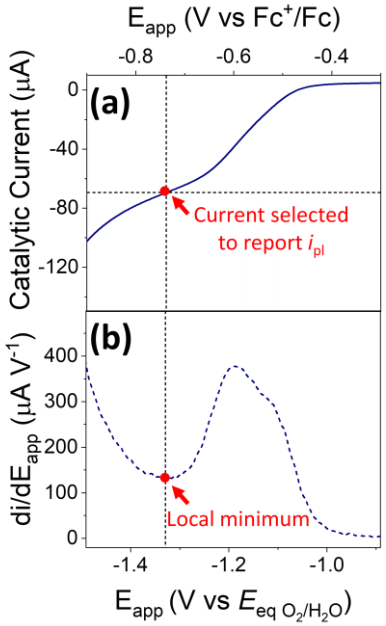

Figure S20. (a) A representative plot of catalytic current versus applied electrode potential recorded under O_2 (1 atm) at a scan rate of 2000 mV s^{-1} (a scan rate more than sufficient to obtain a scan-rate independent response of catalytic currents at adequate electrode bias and as shown in Figures 5b, S17b, S19e, and S19f) using *N,N'*-dimethylformamide solutions containing [$DMFH^+$][OTf^-] (100 mM) as a proton source, $TBAPF_6$ (0.1 M) as a supporting electrolyte, and [FeTTP]Cl (0.14 mM) as a catalyst. A current within the plateau-shaped region of the voltammogram response where the first derivative of the catalytic current yields a local minimum (see panel b) was selected to (1) report the corresponding catalytic plateau current, i_{pl}, and (2) establish a potential for monitoring the catalytic current while varying the scan rate. (b) A first derivative plot of the data shown in panel a, where a second order Savitzky-Golay filter method was used for data smoothing. The catalytic current selected to report the catalytic plateau current, i_{pl}, and establish a potential for monitoring the catalytic current while varying the scan rate, was determined by finding the local minimum of the first derivative (*i.e.*, where the slope of the voltammogram trace becomes closest to zero). In general, a 'faster' catalyst requires faster scan rates to obtain experimental conditions suitable for extracting i_{pl} values and deriving the corresponding TOF_{max} and $E_{cat/2}$ values.

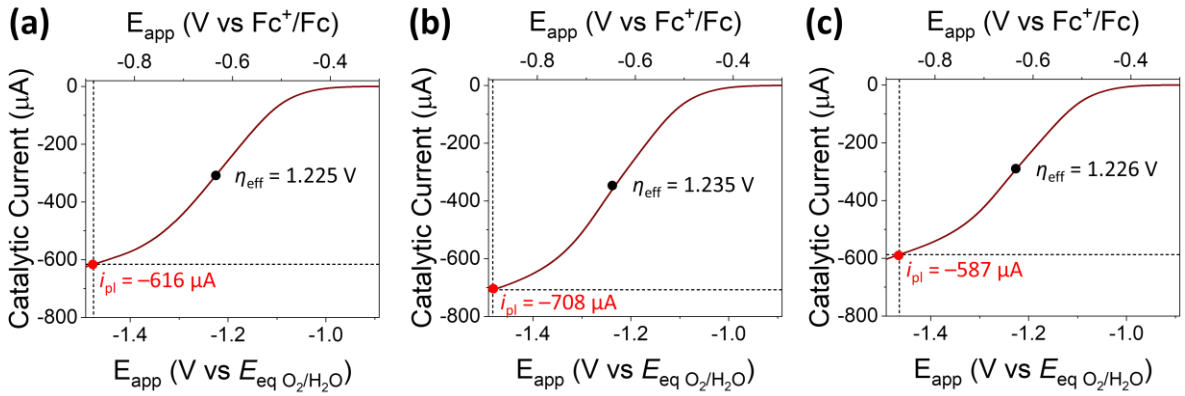

Figure S21. (a–c) Representative plots of catalytic current versus applied electrode potential used to derive the TOF_{max} and $E_{cat/2}$ values of $[Fe_2FP]Cl_2$. All data were recorded under O_2 (1 atm) at scan rates sufficient to yield scan-rate independent, limiting values of the catalytic currents—2500 mV s^{-1} (panels a and b) or 2000 mV s^{-1} (panel c)—when using *N*,*N'*-dimethylformamide solutions containing $[DMFH^+][OTf^-]$ (100 mM) as a proton source, $TBAPF_6$ (0.1 M) as a supporting electrolyte, and $[Fe_2FP]Cl_2$ (0.14 mM) as a catalyst. The catalytic currents selected to report the catalytic plateau currents (i_{pl} values) are indicated via the red dots and black horizontal lines (see Figure S20 for further details). The potentials used to monitor catalytic currents under varying scan rate conditions (see Figures 5c, S17e, S17f, S19a, and S19b) are indicated via the black vertical lines. The effective overpotentials (taken as the catalytic half-wave potential) are indicated via the black dots. The representative plots shown in panels a, b, and c of this figure were recorded at the indicated scan rates, which yielded the highest catalytic plateau current within a given triplicate experimental data set recorded using $[Fe_2FP]Cl_2$ and scan rates ranging from 100 to 2500 mV s^{-1} (see Figures S17e, S17f, and S19). For the related plots of catalytic current versus scan rate shown in Figures S17e, S17f, and S19, the 'faster' catalysts require relatively higher scan rates (as compared to those required for 'slower' catalysts) to approach the scan-rate independent, limiting current region.

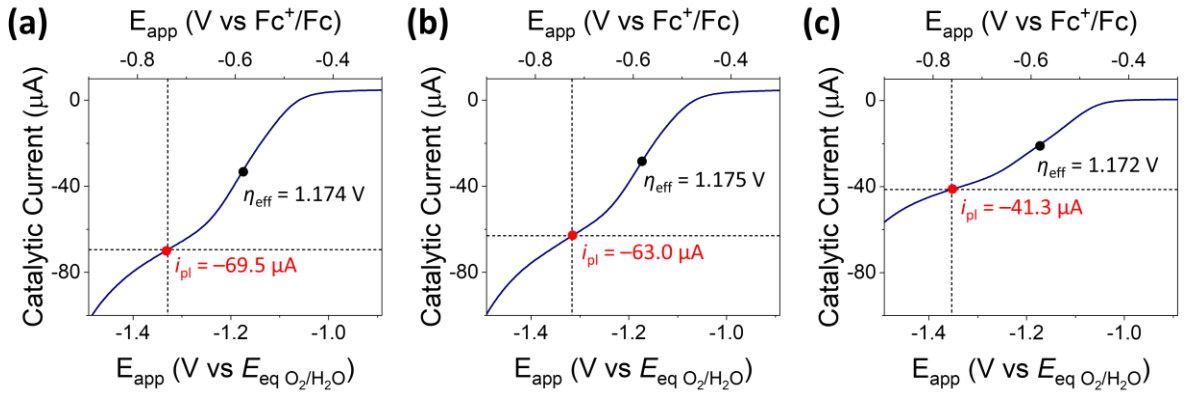

Figure S22. (a–c) Representative plots of catalytic current versus applied electrode potential used to derive TOF_{max} and $E_{cat/2}$ values of [FeTTP]Cl. All data were recorded under O_2 (1 atm) at scan rates sufficient to yield scan-rate independent, limiting values of the catalytic currents—2000 mV s^{-1} (panel a and b) or 500 mV s^{-1} (panel c)—when using *N*,*N'*-dimethylformamide solutions containing $[DMFH^+][OTf^-]$ (100 mM) as a proton source, $TBAPF_6$ (0.1 M) as a supporting electrolyte, and [FeTTP]Cl (0.14 mM) as a catalyst. The catalytic currents selected to report the catalytic plateau currents (i_{pl} values) are indicated via the red dots and black horizontal lines (see Figure S20 for further details). The potentials used to monitor catalytic currents under varying scan rate conditions (see Figures 5c, S17e, S17f, S19e, and S19f) are indicated via the black vertical lines. The effective overpotentials (taken as the catalytic half-wave potential) are indicated via the black dots. The representative plots shown in panels a, b, and c of this figure were recorded at the indicated scan rates, which yielded the highest catalytic plateau current within a given triplicate experimental data set recorded using [FeTTP]Cl and scan rates ranging from 100 to 2500 mV s^{-1} (see Figures S17e, S17f, and S19). For the related plots of catalytic current versus scan rate shown in Figures S17e, S17f, and S19, the 'faster' catalysts require relatively higher scan rates (as compared to those required for 'slower' catalysts) to approach the scan-rate independent, limiting current region.

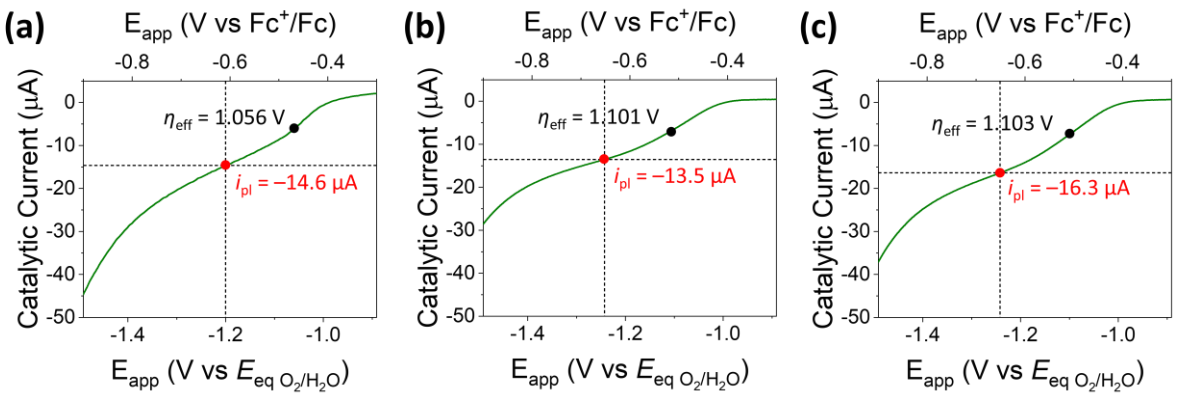

Figure S23. (a–c) Representative plots of catalytic current versus applied electrode potential used to derive TOF_{max} and $E_{cat/2}$ values of [FeT*p*CF_3PP]Cl. All data were recorded under O_2 (1 atm) at a scan rates sufficient to yield scan-rate independent, limiting values of the catalytic currents—2500 mV s^{-1} (panel a) or 100 mV s^{-1} (panels b and c)—when using *N,N'*-dimethylformamide solutions containing [$DMFH^+$][OTf^-] (100 mM) as a proton source, $TBAPF_6$ (0.1 M) as a supporting electrolyte, and [FeT*p*CF_3PP]Cl (0.14 mM) as a catalyst. The catalytic currents selected to report the catalytic plateau currents (i_{pl} values) are indicated via the red dots and black horizontal lines (see Figure S20 for further details). The potentials used to monitor catalytic currents under varying scan rate conditions (see Figures S17e, S17f, S19g, and S19h) are indicated via the black vertical lines. The effective overpotentials (taken as the catalytic half-wave potential) are indicated via the black dots. The representative plots shown in panels a, b, and c of this figure were recorded at the indicated scan rates, which yielded the highest catalytic plateau current within a given triplicate experimental data set recorded using [FeT*p*CF_3PP]Cl and scan rates ranging from 100 to 2500 mV s^{-1} (see Figures S17e, S17f, and S19). For the related plots of catalytic current versus scan rate shown in Figures S17e, S17f, and S19, the 'faster' catalysts require relatively higher scan rates (as compared to those required for 'slower' catalysts) to approach the scan-rate independent, limiting current region.

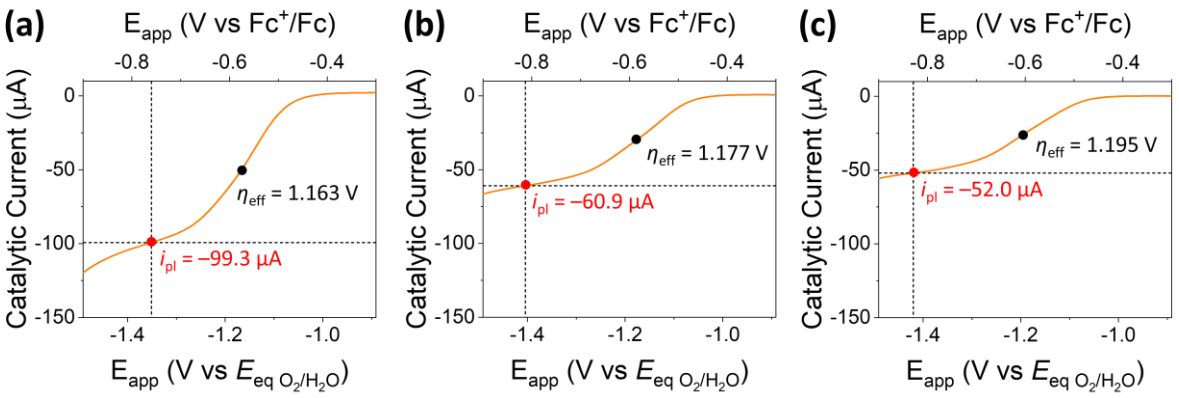

Figure S24. (a–c) Representative plots of catalytic current versus applied electrode potential used to derive TOF_{max} and $E_{cat/2}$ values of [FeT*p*OMePP]Cl. All data were recorded under O_2 (1 atm) at a scan rates sufficient to yield scan-rate independent, limiting values of the catalytic currents—2000 mV s^{-1} (panel a), 1000 mV s^{-1} (panel b), or 500 mV s^{-1} (panel c)—when using *N*,*N'*-dimethylformamide solutions containing [$DMFH^+$][OTf^-] (100 mM) as a proton source, $TBAPF_6$ (0.1 M) as a supporting electrolyte, and [FeT*p*OMePP]Cl (0.14 mM) as a catalyst. The catalytic currents selected to report the catalytic plateau currents (i_{pl} values) are indicated via the red dots and black horizontal lines (see Figure S20 for further details). The potentials used to monitor catalytic currents under varying scan rate conditions (see Figures S17e, S17f, S19c, and S19d) are indicated via the black vertical lines. The effective overpotentials (taken as the catalytic half-wave potential) are indicated via the black dots. The representative plots shown in panels a, b, and c of this figure were recorded at the indicated scan rates, which yielded the highest catalytic plateau current within a given triplicate experimental data set recorded using [FeT*p*OMePP]Cl and scan rates ranging from 100 to 2500 mV s^{-1} (see Figures S17e, S17f, and S19). For the related plots of catalytic current versus scan rate shown in Figures S17e, S17f, and S19, the 'faster' catalysts require relatively higher scan rates (as compared to those required for 'slower' catalysts) to approach the scan-rate independent, limiting current region.

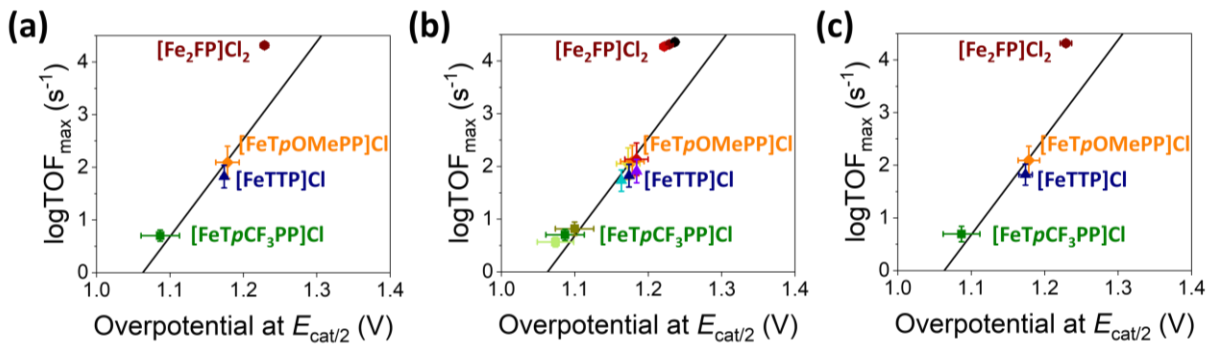

Figure S25. (a) $\log TOF_{max}$ versus overpotential at $E_{cat/2}$ plot presented as Figure 6b in the main text. In this plot, the values of TOF_{max} and $E_{cat/2}$ were calculated using the catalytic currents selected to report the catalytic plateau currents, i_{pl} values (as determined using the first derivative of the voltammogram traces and as further described in the caption of Figure S20 and the Experimental Section of the main text). Here, the data points represent average values obtained from triplicate voltammetry experiments for each catalyst. By extension, the error bars represent the standard deviations of three measurements to derive each TOF_{max} and $E_{cat/2}$ value. (b) $\log TOF_{max}$ versus overpotential at $E_{cat/2}$ plot, where the values of TOF_{max} and $E_{cat/2}$ were calculated using either (1) the catalytic current selected to report the catalytic plateau current, i_{pl}, as determined using the local minima obtained from first derivative plots of the voltammograms (red, blue, green, or orange data points and error bars; this is the same approach used for the data plotted in panel a and included here in panel b for comparison), (2) the catalytic current 50 mV positive of the local minima obtained from first derivative plots of the voltammograms (light brown, light blue, light green, and yellow data points and error bars), or (3) the catalytic current 50 mV negative of the local minima obtained from first derivative plots of the voltammograms (black, purple, dark yellow, and dark red data points and error bars). (c) $\log TOF_{max}$ versus overpotential at $E_{cat/2}$ plot, where the values of TOF_{max} and $E_{cat/2}$ were calculated as average values of the nine TOF_{max} and nine $E_{cat/2}$ indicated in pane b. By extension, the error bars represent the standard deviations of the nine TOF_{max} and nine $E_{cat/2}$ values used to construct the plot shown in panel b. The overlapping error bars associated with the $\log TOF_{max}$ versus $E_{cat/2}$ plots in panels a, b, and c show that choosing values within 100 mV span of the catalytic plateau current region does not have a major effect on the values of $\log TOF_{max}$ or $E_{cat/2}$. However, the approach of using local minima obtained from first derivative plots of the voltammograms does provide a consistent approach for reporting purposes.

5.5. Effects of catalyst concentration on catalytic activity

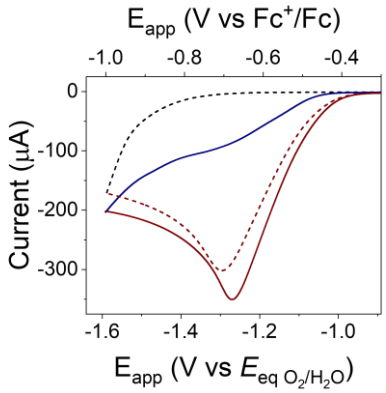

Figure S26. Voltammograms recorded under O_2 (1 atm) using *N,N'*-dimethylformamide solutions containing either $[Fe_2FP]Cl_2$ (0.15 mM) (red dash), $[Fe_2FP]Cl_2$ (0.30 mM) (red solid), or [FeTTP]Cl (0.30 mM) (blue solid) as a catalyst. A voltammogram recorded in the absence of a catalyst (black dash) is included for comparison. All data were recorded at a scan rate of 100 mV s^{-1} using solutions containing $[DMFH^+][OTf^-]$ (100 mM) as a proton source and $TBAPF_6$ (0.1 M) as a supporting electrolyte. These control experiments indicate that the enhanced electrocatalytic activity of the fused porphyrin is not due to a simple doubling of the iron site concentration for solutions that are equimolar in porphyrin.

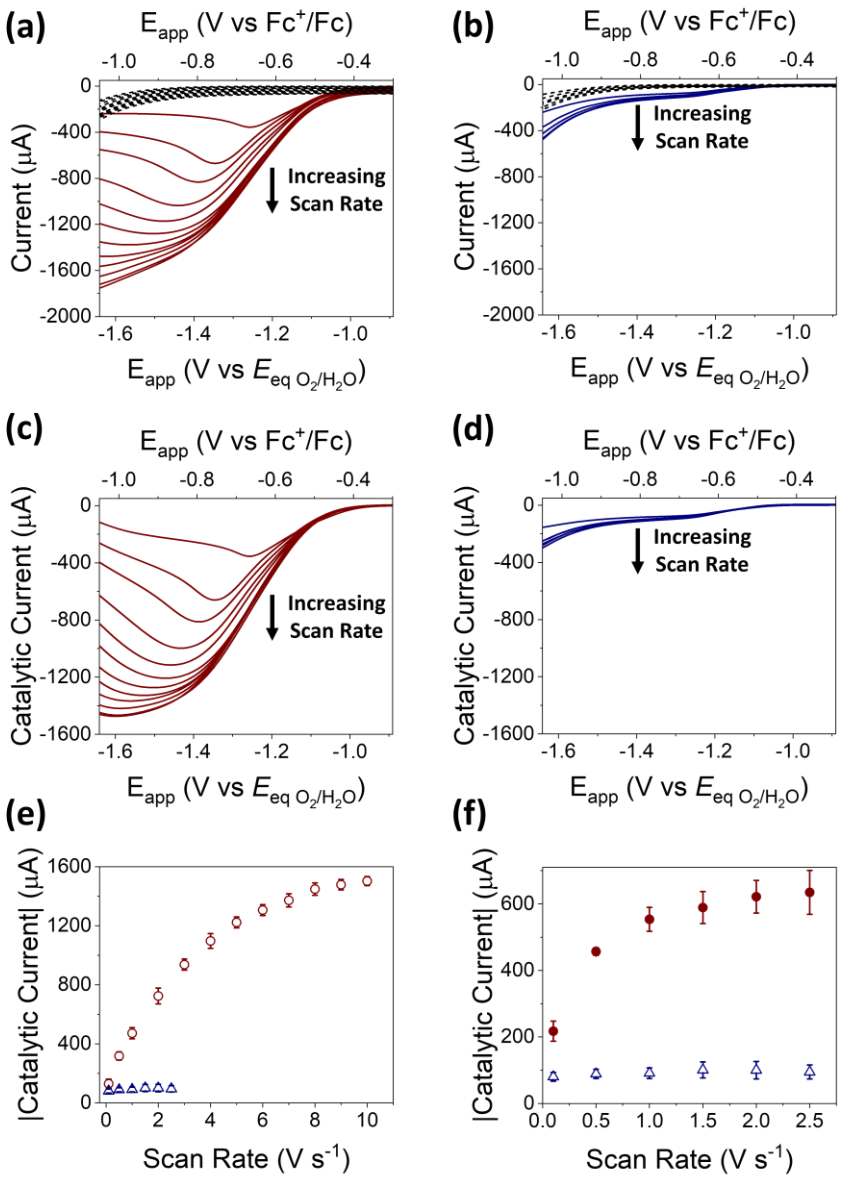

Figure S27. (a) Voltammograms recorded under O_2 (1 atm) with increasing scan rates (100, 500, 1000, 2000, 3000, 4000, 5000, 6000, 7000, 8000, 9000, and 10000 mV s^{-1}) using *N,N'*-dimethylformamide solutions containing a relatively high concentration of $[Fe_2FP]Cl_2$ (0.27 mM) (red). Voltammograms recorded in the absence of a catalyst (black dash) are included for comparison. All solutions contained $[DMFH^+][OTf^-]$ (100 mM) as a proton source and $TBAPF_6$ (0.1 M) as a supporting electrolyte. (b) Voltammograms recorded under O_2 (1 atm) and with increasing scan rates (100, 500, 1000, 1500, 2000, and 2500 mV s^{-1}) using *N,N'*-dimethylformamide solutions containing a relatively high concentration of [FeTTP]Cl (0.27 mM) (blue). Voltammograms recorded in the absence of a catalyst (black dash) are included for comparison. All solutions contained $[DMFH^+][OTf^-]$ (100 mM) as a proton source and $TBAPF_6$ (0.1 M) as a supporting electrolyte. (c) Catalytic current versus applied electrode potential plots obtained from voltammetry measurements (see panel a) using a relatively high concentration of $[Fe_2FP]Cl_2$ (0.27 mM) (red). (d) Catalytic current versus applied electrode potential plots obtained from voltammetry measurements (see panel b) using a relatively high concentration of [FeTTP]Cl (0.27 mM)

(blue). (e) Catalytic current versus scan rate plots obtained from voltammetry measurements (see panels a and b) performed using either a relatively high concentration of $[Fe_2FP]Cl_2$ (0.27 mM) (open red circles) or a relatively high concentration of [FeTTP]Cl (0.27 mM) (open blue triangles) as a catalyst. In these plots, the catalytic currents are reported at potentials determined via analyzing the first derivative of corresponding voltammograms (see the Experimental Section of the main text and Section 5.4 of this Supporting Information file for details). Consistent with the compass rose of kinetic zone diagrams,[37,39] voltammograms recorded using relatively high concentrations of catalysts are less likely to achieve "S-shaped" waveforms and exhibit deviation from "pure kinetic conditions" and "Zone KS".[37,39] The catalytic current versus applied electrode potential plots obtained from voltammograms recorded at 10000 mV s^{-1} and using 0.27 mM in $[Fe_2FP]Cl_2$ electrolyte solutions did not permit a determination of the current to report i_{pl} via the first derivative analysis used elsewhere in this work. Thus, for samples containing a relatively high concentration of $[Fe_2FP]Cl_2$ (0.27 mM), the peak catalytic current intensities recorded at 10000 mV s^{-1} were used to establish a potential for monitoring the catalytic current while varying the scan rate and constructing the corresponding plot. (f) Catalytic current versus scan rate plots obtained from voltammetry measurements (see Figures 5a, S17a, and panel b of this figure) performed using a relatively low concentration of $[Fe_2FP]Cl_2$ (0.14 mM) (closed red circles and using the same data plotted in Figures 5c and S17e) or a relatively high concentration of [FeTTP]Cl (0.27 mM) (open blue triangles and using the same data plotted in panel e of this figure) as a catalyst. In these plots, the catalytic currents are reported at potentials determined via analyzing the first derivative of corresponding voltammograms (see the Experimental Section of the main text and Section 5.4 of this Supporting Information file for details).

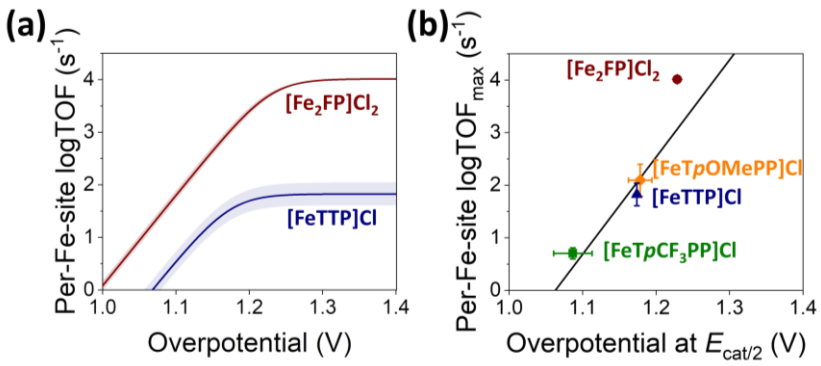

Figure S28. (a) Per-iron-site logTOF versus overpotential plots constructed from the values of TOF_{max} and $E_{cat/2}$ recorded using *N,N'*-dimethylformamide solutions containing $[Fe_2FP]Cl_2$ (0.14 mM) (red), where the TOF_{max} is divided by two to account for the presence of two iron sites per catalyst unit, or [FeTTP]Cl (0.14 mM) (blue), where there is single iron site per catalyst unit and thus the $logTOF_{max}$ is equivalent to the per-iron-site $logTOF_{max}$. All data were recorded in the presence of O_2 (1 atm), $[DMFH^+][OTf^-]$ (100 mM), and $TBAPF_6$ (0.1 M). The shaded areas indicate the standard deviations from the mean values. Overpotential is calculated using a 20 mM concentration of water in *N,N'*-dimethylformamide. (b) $logTOF_{max}$ versus overpotential at $E_{cat/2}$ plot constructed using data included in panel a for $[Fe_2FP]Cl_2$ (red circle) or [FeTTP]Cl (blue triangle). Data obtained using [FeT*p*CF_3PP]Cl, a porphyrin catalyst featuring electron-withdrawing fluorine groups, (green square) or [FeT*p*OMePP]Cl, a porphyrin catalyst featuring electron-donating methoxy groups, (orange diamond) are included for comparison. The error bars indicate standard deviations from the mean values. The black line with a slope of 54 mV/dec (black) indicates a traditional scaling relationship for benchmarking a related series of iron porphyrin oxygen reduction reaction catalysts.[35,40–43] The benchmarks for $[Fe_2FP]Cl_2$ break the scaling relationship and deviate from the correlation slope even after the TOF_{max} of $[Fe_2FP]Cl_2$ is divided by two to yield the per-iron-site TOF_{max}.

5.6. Effect of water

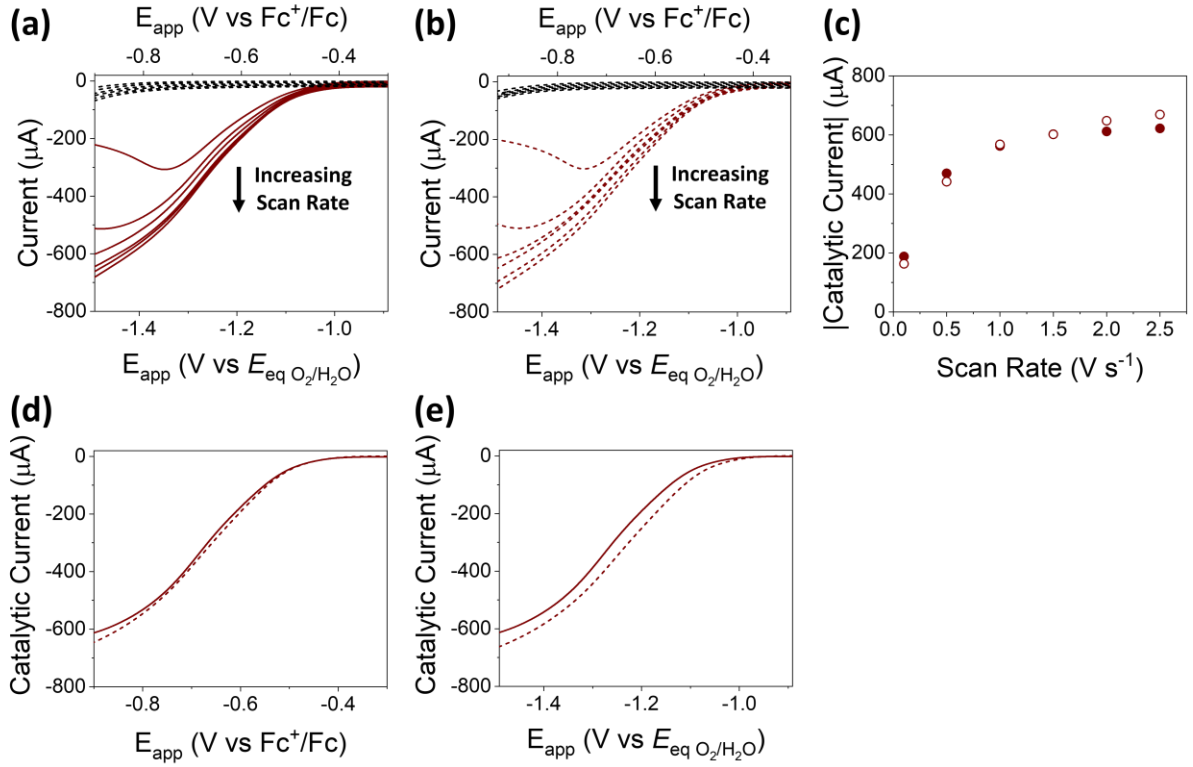

Figure S29. (a) and (b) Voltammograms recorded under O_2 (1 atm) and at increasing scan rates (100, 500, 1000, 1500, 2000, and 2500 mV s^{-1}) using *N,N'*-dimethylformamide solutions containing $[Fe_2FP]Cl_2$ (0.14 mM) either in the absence of added water (panel a, red solid) ($[H_2O]$ = 20 mM) or presence of added water (panel b, red dash) ($[H_2O]$ = 120 mM). Voltammograms recorded in the absence of a catalyst (black dash) are included for comparison. All solutions contained $[DMFH^+][OTf^-]$ (100 mM) as a proton source and $TBAPF_6$ (0.1 M) as a supporting electrolyte. (c) Catalytic current versus scan rate plots obtained from voltammetry measurements using $[Fe_2FP]Cl_2$ (0.14 mM) as a catalyst and recorded either in the presence (closed circles) or absence (open circles) of added water and under varying scan rates. In these plots, the catalytic currents are reported at potentials determined via analyzing the first derivative of corresponding voltammograms (see the Experimental Section of the main text and Section 5.4 of this Supporting Information file for details). (d) and (e) Catalytic current versus applied electrode potential plots obtained from voltammetry measurements (see panels a and b) performed under O_2 (1 atm) at a scan rate of 2500 mV s^{-1} using *N,N'*-dimethylformamide solutions containing $[Fe_2FP]Cl_2$ (0.14 mM) as a catalyst either in the absence of added water (solid) or presence of added water (dash). The applied electrode potential is reported with respect to the ferrocenium/ferrocene redox couple (Fc^+/Fc) (panel d) or the equilibrium potential of the oxygen reduction to form water ($E_{eq\ O_2/H_2O}$) (panel e). These results indicate the effects of varying water concentrations in *N,N'*-dimethylformamide solutions would not affect the general trends in catalytic activity for the complexes reported herein or alter our overall interpretations.

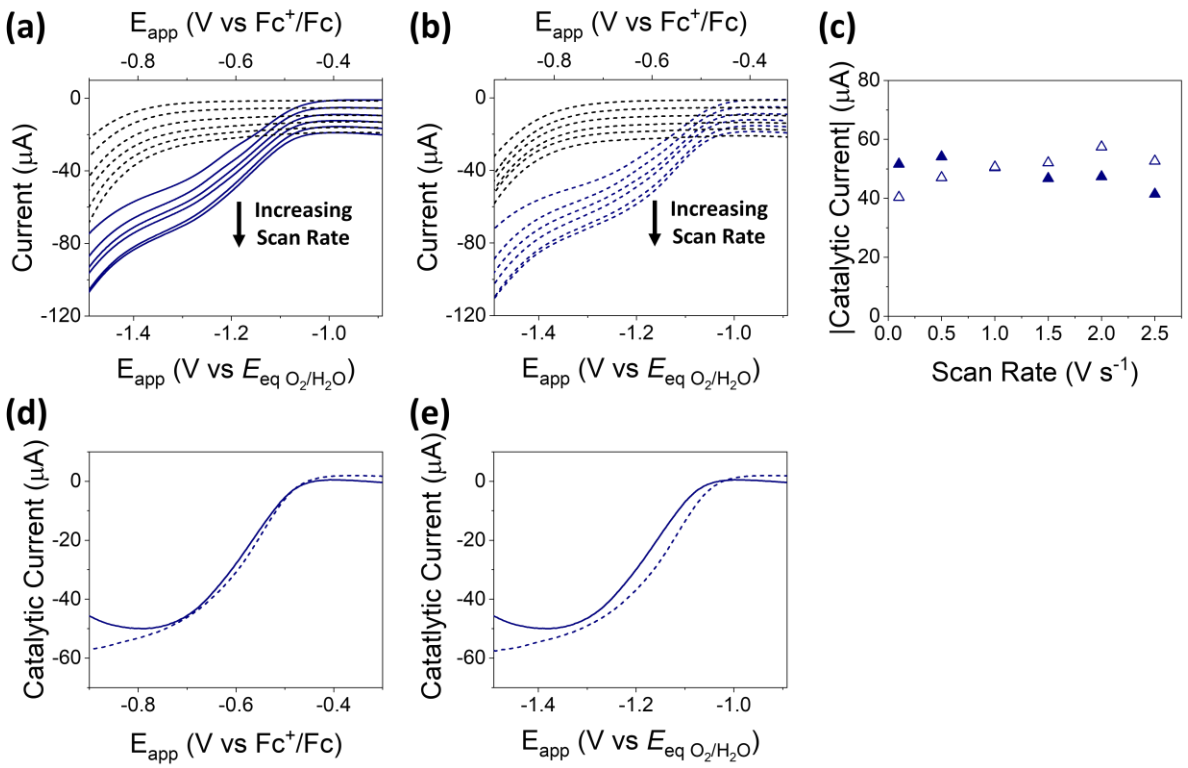

Figure S30. (a) and (b) Voltammograms recorded under O_2 (1 atm) and at increasing scan rates (100, 500, 1000, 1500, 2000, and 2500 mV s^{-1}) using *N,N'*-dimethylformamide solutions containing [FeTTP]Cl (0.14 Mm) either in the absence of added water (panel a, blue solid) ([H_2O] = 20 mM) or presence of added water (panel b, blue dash) ([H_2O] = 120 mM). Voltammograms recorded in the absence of a catalyst (black dash) are included for comparison. All solutions contained [$DMFH^+$][OTf^-] (100 mM) as a proton source and $TBAPF_6$ (0.1 M) as a supporting electrolyte. (c) Catalytic current versus scan rate plots obtained from voltammetry measurements using [FeTTP]Cl (0.14 mM) as a catalyst and recorded either in the presence (closed triangles) or absence (open triangles) of added water and under varying scan rates. In these plots, the catalytic currents are reported at potentials determined via analyzing the first derivative of corresponding voltammograms (see the Experimental Section of the main text and Section 5.4 of this Supporting Information file for details). (d) and (e) Catalytic current versus applied electrode potential plots obtained from voltammetry measurements (see panels a and b) performed under O_2 (1 atm) at a scan rate of 2000 mV s^{-1} using *N,N'*-dimethylformamide solutions containing [FeTTP]Cl (0.14 mM) as a catalyst either in the absence of added water (solid) or in the presence of added water (dash). The applied electrode potential is reported with respect to the ferrocenium/ferrocene redox couple (Fc^+/Fc) (panel d) or the equilibrium potential of the oxygen reduction to form water ($E_{\mathrm{eq}\,O_2/H_2O}$) (panel e). These results indicate the effects of varying water concentrations in *N,N'*-dimethylformamide solutions would not affect the general trends in catalytic activity for the complexes reported herein or alter our overall interpretations.

6. Rotating ring-disk electrode experiments

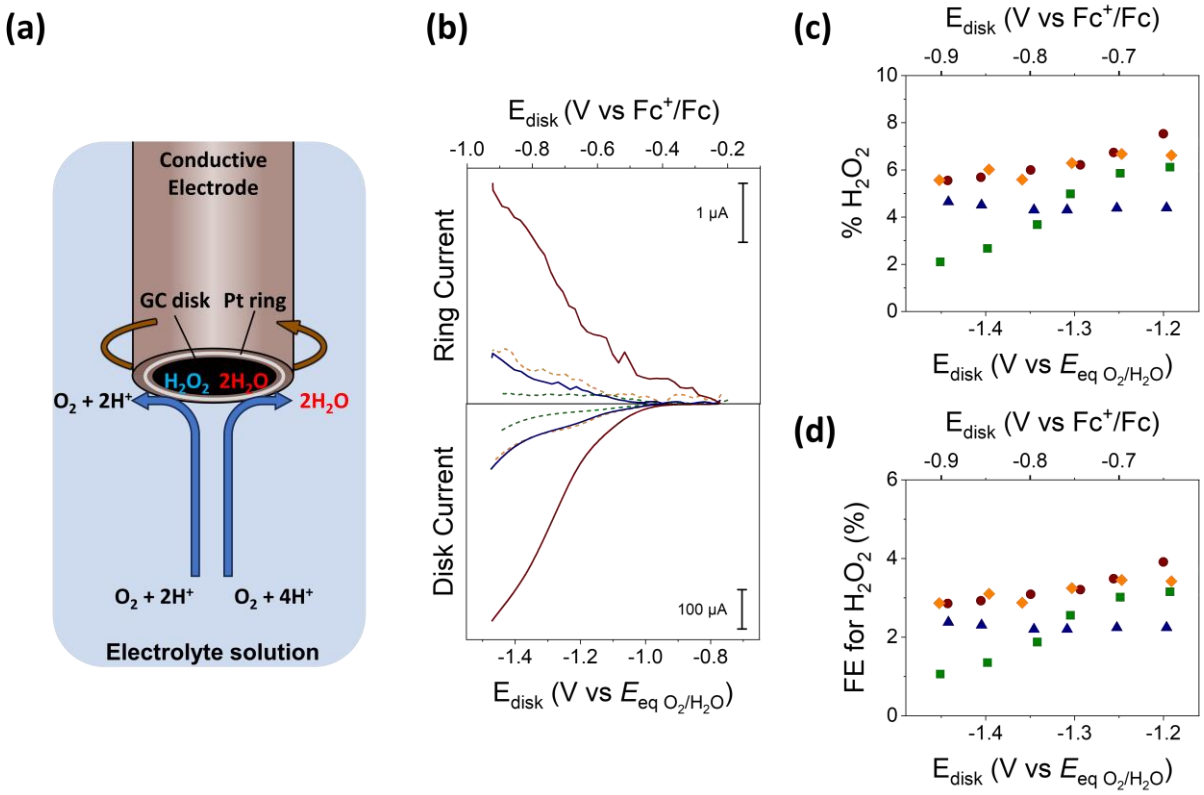

Figure S31. (a) Schematic illustration of a rotating ring disk electrode experiment, where O_2 and H^+ are reduced into H_2O or H_2O_2 at a glassy carbon disk electrode to generate cathodic current at the disk electrode (i_{disk}). These products (H_2O or H_2O_2) are then transported to a platinum ring electrode that is polarized at a potential where only the H_2O_2 is oxidized and generates an anodic current at the platinum ring electrode (i_{ring}). (b) Voltammograms recorded under O_2 (1 atm) using *N,N'*-dimethylformamide solutions containing either $[Fe_2FP]Cl_2$ (0.1 mM) (red solid), [FeTTP]Cl (0.1 mM) (blue solid), [FeT*p*CF_3PP]Cl (0.1 mM) (green dash), or [FeT*p*OMePP]Cl (0.1 mM) (orange dash) as a catalyst and $[DMFH^+][OTf^-]$ (20 mM) as a proton source. All data were recorded at a scan rate of 100 mV s^{-1} using solutions containing $TBAPF_6$ (0.1 M) as a supporting electrolyte and a 5 mm diameter glassy carbon working disk electrode rotating at 1000 rpm. Currents at the disk electrode were recorded while the applied electrode potential at the disk electrode (E_{disk}) was swept cathodically, whereas currents at the platinum ring electrode were recorded while the applied electrode potential at the platinum ring electrode (E_{ring}) was set to +0.05 V vs $E_{eq\ O_2/H_2O}$. (c) $\%H_2O_2$ versus applied disk potential plots obtained using data shown in panel a for $[Fe_2FP]Cl_2$ (0.1 mM) (red circles), [FeTTP]Cl (0.1 mM) (blue triangles), [FeT*p*CF_3PP]Cl (0.1 mM) (green squares), or [FeT*p*OMePP]Cl (0.1 mM) (orange diamonds). The reported $\%H_2O_2$ values may involve systematic errors arising from the sluggish H_2O_2 oxidation kinetics at the platinum ring.[44] To avoid the complexity of the analysis, these effects were not eliminated. (d) Faradaic efficiency (*FE*) for H_2O_2 versus applied disk potential plots constructed using data shown in panel a for $[Fe_2FP]Cl_2$ (0.1 mM) (red circles), [FeTTP]Cl (0.1 mM) (blue triangles), [FeT*p*CF_3PP]Cl (0.1 mM) (green squares), or [FeT*p*OMePP]Cl (0.1 mM) (orange diamonds).

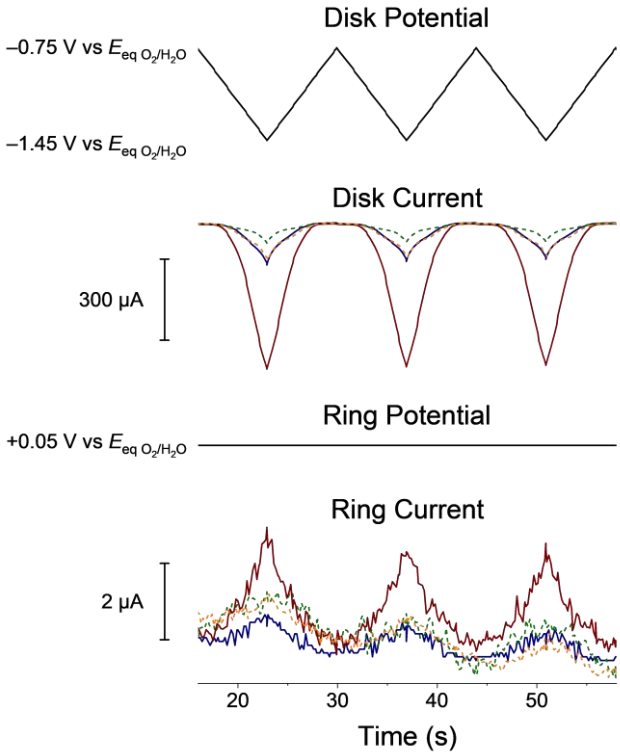

Figure S32. Rotating ring-disk electrode data recorded under O_2 (1 atm) at a scan rate of 100 mV s^{-1} and using either [Fe_2FP]Cl_2 (0.1 mM) (red solid), [FeTTP]Cl (0.1 mM) (blue solid), [FeT*p*CF_3PP]Cl (0.1 mM) (green dash), or [FeT*p*OMePP]Cl (0.1 mM) (orange dash) as a catalyst, *N*,*N'*-dimethylformamide solutions containing [$DMFH^+$][OTf^-] (20 mM) as a proton source, $TBAPF_6$ (0.1 M) as a supporting electrolyte, and a 5 mm diameter glassy carbon working disk electrode rotating at 1000 rpm.

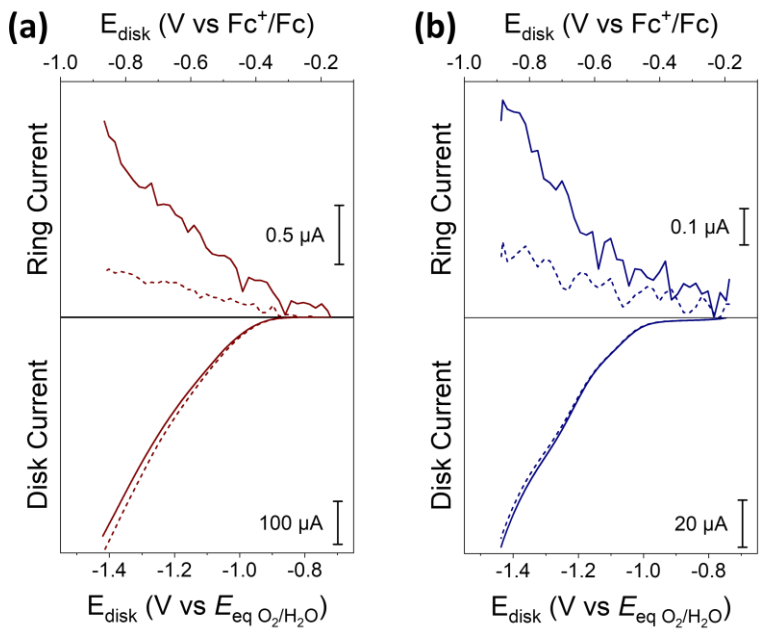

Figure S33. (a) Voltammograms recorded under O_2 (1 atm) using *N*,*N'*-dimethylformamide solutions containing $[Fe_2FP]Cl_2$ (0.1 mM) as a catalyst, $[DMFH^+][OTf^-]$ (20 mM) as a proton source, and $TBAPF_6$ (0.1 M) as a supporting electrolyte. The current at the disk electrode (i_{disk}) was recorded while the applied electrode potential at the disk electrode (E_{disk}) was swept cathodically. Conversely, the current at the platinum ring electrode (i_{ring}) was recorded while the applied electrode potential at the platinum ring electrode (E_{ring}) was polarized at a constant potential of either –0.59 V vs $E_{eq\ O_2/H_2O}$ (red dash) or +0.21 V vs $E_{eq\ O_2/H_2O}$ (red solid). At –0.59 V vs $E_{eq\ O_2/H_2O}$, $[Fe_2FP]^0$ is oxidized to $[Fe_2FP]^{2+}$, but H_2O_2 is not oxidized. At +0.21 V vs $E_{eq\ O_2/H_2O}$, both $[Fe_2FP]^0$ and H_2O_2 are oxidized. No substantial ring current was observed when the platinum ring electrode was polarized at –0.59 V vs $E_{eq\ O_2/H_2O}$, indicating that H_2O_2, not $[Fe_2FP]^0$, is the source of the ring current when the platinum ring is polarized at +0.21 V vs $E_{eq\ O_2/H_2O}$. (b) Voltammograms recorded under O_2 (1 atm) using *N*,*N'*-dimethylformamide solutions containing [FeTTP]Cl (0.1 mM) as a catalyst and $[DMFH^+][OTf^-]$ (20 mM) as a proton source. i_{disk} was recorded while E_{disk} was swept cathodically. Conversely, i_{ring} was recorded while E_{ring} was polarized at a constant potential of either –0.61 V vs $E_{eq\ O_2/H_2O}$ (blue dash) or +0.19 V (blue solid). At –0.61 V vs $E_{eq\ O_2/H_2O}$, $[FeTTP]^0$ is oxidized to $[FeTTP]^+$, but H_2O_2 is not oxidized. At +0.19 V vs $E_{eq\ O_2/H_2O}$, both $[FeTTP]^0$ and H_2O_2 are oxidized. No substantial ring current was observed when the Pt ring was polarized at –0.61 V vs $E_{eq\ O_2/H_2O}$, indicating that H_2O_2, not $[FeTTP]^0$, is the source of the ring current when the platinum ring electrode is polarized at +0.19 V vs $E_{eq\ /H_2O}$. All data were recorded at a scan rate of 100 mV s^{-1} using a 5 mm diameter glassy carbon working disk electrode rotating at 1000 rpm.

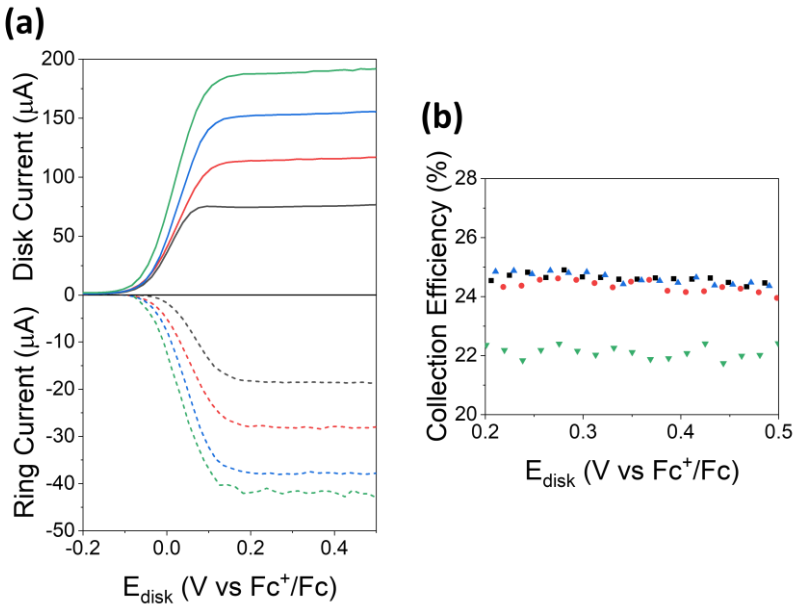

Figure S34. (a) Voltammograms recorded under argon using *N,N'*-dimethylformamide solutions containing ferrocene (1 mM) and $TBAPF_6$ (0.1 M) as a supporting electrolyte. All data were recorded at a scan rate of 100 mV s^{-1} using a 5 mm diameter glassy carbon working disk electrode rotating at 400 (black), 900 (red), 1600 (blue), and 2500 (green) rpm. The current at the disk electrode (i_{disk}, solid) was recorded while the applied electrode potential at the disk electrode (E_{disk}) was swept anodically. Conversely, the current at the platinum ring electrode (i_{ring}, dash) was recorded while the applied electrode potential at the platinum ring electrode was polarized at a constant value of –0.3 V vs Fc^+/Fc. (b) Collection efficiency of the rotating ring-disk electrode assembly versus biased disk potential constructed using the data shown in panel a.

7. Summary

Table S7. Summary of electrochemical ORR catalysis by iron porphyrins.

	TOF_{max} (s^{-1})	**η at $E_{cat/2}$ (V)**	**$E_{cat/2}$ (V vs Fc^+/Fc)**	**E of the $Fe^{III/II}$ redox couples[a] (V vs Fc^+/Fc)**	**$\%H_2O_2$/ $\%H_2O$[d]**	***FE* for H_2O_2/H_2O[d]**
$[Fe_2FP]Cl_2$	$(2.06 \pm 0.03) \times 10^4$	1.229 ± 0.006	–0.638 ± 0.006	–0.71[b] / –0.76[c] –0.56[b] / –0.64[c]	6.3% / 93.7%	3.3% / 96.7%
[FeTTP]Cl	$(7 \pm 3) \times 10^1$	1.174 ± 0.002	–0.583 ± 0.002	–0.56[b] / –0.73[c]	4.5% / 95.5%	2.3% / 97.7%
[FeT*p*CF_3PP]Cl	5 ± 1	1.09 ± 0.03	–0.50 ± 0.03	–0.55[b] / –0.64[c]	4.1% / 95.9%	2.1% / 97.9%
[FeT*p*OMePP]Cl	$(1.4 \pm 0.8) \times 10^2$	1.18 ± 0.02	–0.59 ± 0.02	–0.58[b] / –0.74[c]	6.2% / 93.8%	3.2% / 96.8%

[a]Peak potentials of the first or second redox couple observed in the absence of a chemical substrate

[b]*E* = anodic peak potential; electrochemically irreversible

[c]*E* = cathodic peak potential; electrochemically irreversible

[d]Averaged values over the potential range between –1.2 and –1.45 V vs $E_{\mathrm{eq}\,O_2/H_2O}$, where $\%H_2O$ is calculated using 100% – $\%H_2O_2$, assuming that the total *FE* of ORR is 100% and that H_2O_2 and H_2O are the only products.[45,46]

8. References

(1) Smith, P. W. G.; Tatchell, A. R. Aromatic Condensed Ring Systems. In *Aromatic Chemistry*; Elsevier Ltd, 1969; pp 196–221.

(2) McCormack, A. C.; McDonnell, C. M.; More O'Ferrall, R. A.; O'Donoghue, A. M. C.; Rao, S. N. Protonated Benzofuran, Anthracene, Naphthalene, Benzene, Ethene, and Ethyne: Measurements and Estimates of pK_a and pK_R. *J. Am. Chem. Soc.* **2002**, *124*, 8575–8583.

(3) Reyes Cruz, E. A.; Nishiori, D.; Wadsworth, B. L.; Khusnutdinova, D.; Karcher, T.; Landrot, G.; Lassalle-Kaiser, B.; Moore, G. F. Six-Electron Chemistry of a Binuclear Fe(III) Fused Porphyrin. *ChemElectroChem* **2021**, *8*, 3614–3620.

(4) Lindsey, J. S.; Hsu, H. C.; Schreiman, I. C. Synthesis of Tetraphenylporphyrins under Very Mild Conditions. *Tetrahedron Lett.* **1986**, *27*, 4969–4970.

(5) Kooriyaden, F. R.; Sujatha, S.; Arunkumar, C. Synthesis, Spectral, Structural and Antimicrobial Studies of Fluorinated Porphyrins. *Polyhedron* **2015**, *97*, 66–74.

(6) Tabor, E.; Połtowicz, J.; Pamin, K.; Basąg, S.; Kubiak, W. Influence of Substituents in meso-Aryl Groups of Iron μ-Oxo Porphyrins on Their Catalytic Activity in the Oxidation of Cycloalkanes. *Polyhedron* **2016**, *119*, 342–349.

(7) Adler, A. D.; Longo, F. R.; Finarelli, J. D.; Goldmacher, J.; Assour, J.; Korsakoff, L. A Simplified Synthesis for *meso*-Tetraphenylporphine. *J. Org. Chem.* **1967**, *32*, 476.

(8) Barnett, G. H.; Hudson, M. F.; Smith, K. M. Concerning *meso*-Tetraphenylporphyrin Purification. *J. Chem. Soc. Perkin Trans. 1* **1975**, 1401–1403.

(9) Asano, N.; Uemura, S.; Kinugawa, T.; Akasaka, H.; Mizutani, T. Synthesis of Biladienone and Bilatrienone by Coupled Oxidation of Tetraarylporphyrins. *J. Org. Chem.* **2007**, *72*, 5320–5326.

(10) Wilkinson, A. D.; McNaught, A. *IUPAC Compendium of Chemical Terminology*, 3rd ed.; International Union of Pure and Applied Chemistry: Online version 3.0.1, 2019.

(11) Tsuda, A.; Furuta, H.; Osuka, A. Syntheses, Structural Characterizations, and Optical and Electrochemical Properties of Directly Fused Diporphyrins. *J. Am. Chem. Soc.* **2001**, *123*, 10304–10321.

(12) Sugiura, K.; Matsumoto, T.; Ohkouchi, S.; Naitoh, Y.; Kawai, T.; Takai, Y. Synthesis of the Porphyrin-Fused Porphyrin, [2]Porphyracene. *Chem. Commun.* **1999**, 1957–1958.

(13) Kim, D.; Osuka, A. Photophysical Properties of Directly Linked Linear Porphyrin Arrays. *J. Phys. Chem. A* **2003**, *107*, 8791–8816.

(14) Tanaka, T.; Osuka, A. Conjugated Porphyrin Arrays: Synthesis, Properties and Applications for Functional Materials. *Chem. Soc. Rev.* **2015**, *44*, 943–969.

(15) Khusnutdinova, D.; Wadsworth, B. L.; Flores, M.; Beiler, A. M.; Reyes Cruz, E. A.; Zenkov, Y.; Moore, G. F. Electrocatalytic Properties of Binuclear Cu(II) Fused Porphyrins for Hydrogen Evolution. *ACS Catal.* **2018**, *8*, 9888–9898.

(16) Ali, M. H. F.; Bengasi, G.; Baba, K.; Boscher, N. D. Fused Porphyrin Thin Films as Heterogeneous Visible-Light Active Photocatalysts with Well-Defined Active Metal Sites for Hydrogen Generation. *ACS Appl. Energy Mater.* **2020**, *3*, 9848–9855.

(17) Hazari, A. S.; Chandra, S.; Kar, S.; Sarkar, B. Metal Complexes of Singly, Doubly and Triply Linked Porphyrins and Corroles: An Insight into the Physicochemical Properties. *Chem. Eur. J.* **2022**, *28*, e202104550.

(18) Lexa, D.; Rentien, P.; Savéant, J.-M.; Xu, F. Methods for Investigating the Mechanistic and Kinetic Role of Ligand Exchange Reactions in Coordination Electrochemistry: Cyclic

Voltammetry of Chloroiron(III)Tetraphenylporphyrin in Dimethylformamide. *J. Electroanal. Chem. Interfacial Electrochem.* **1985**, *191*, 253–279.

(19) Lexa, D.; Mispelter, J.; Savéant, J.-M. Electroreductive Alkylation of Iron in Porphyrin Complexes. Electrochemical and Spectral Characteristics of σ-Alkyliron Porphyrins. *J. Am. Chem. Soc.* **1981**, *103*, 6806–6812.

(20) Lexa, D.; Savéant, J.-M.; Wang, D. L. Electroreductive Alkylation of Iron Porphyrins. Iron(III), Iron(II), and Iron(I) Alkyl Complexes from the Reaction of Doubly Reduced Iron(II) Porphyrins with Alkyl Halides. *Organometallics* **1986**, *5*, 1428–1434.

(21) Kadish, K. M.; Van Caemelbecke, E. Electrochemistry of Porphyrins and Related Macrocycles. *J. Solid State Electrochem.* **2003**, *7*, 254–258.

(22) Sun, H.; Smirnov, V. V; DiMagno, S. G. Slow Electron Transfer Rates for Fluorinated Cobalt Porphyrins: Electronic and Conformational Factors Modulating Metalloporphyrin ET. *Inorg. Chem.* **2003**, *42*, 6032–6040.

(23) Lyaskovskyy, V.; de Bruin, B. Redox Non-Innocent Ligands: Versatile New Tools to Control Catalytic Reactions. *ACS Catal.* **2012**, *2*, 270–279.

(24) Luca, O. R.; Crabtree, R. H. Redox-Active Ligands in Catalysis. *Chem. Soc. Rev.* **2013**, *42*, 1440–1459.

(25) Wu, Y.; Jiang, J.; Weng, Z.; Wang, M.; Broere, D. L. J.; Zhong, Y.; Brudvig, G. W.; Feng, Z.; Wang, H. Electroreduction of CO_2 Catalyzed by a Heterogenized Zn–Porphyrin Complex with a Redox-Innocent Metal Center. *ACS Cent. Sci.* **2017**, *3*, 847–852.

(26) Senge, M. O.; Macgowan, A.; Brien, J. M. O. Conformational Control of Cofactors in Nature – the Influence of Protein-Induced Macrocycle Distortion on the Biological Function of Tetrapyrroles. *Chem Commn* **2015**, *51*, 17031–17063.

(27) Sugimoto, M.; Kuramochi, Y.; Satake, A. Measurement of Solvation Ability of Solvents by Porphyrin-Based Solvation / Desolvation Indicators. *ACS Omega* **2020**, *5*, 6045–6050.

(28) Drain, C. M.; Gentemann, S.; Roberts, J. A.; Nelson, N. Y.; Medforth, C. J.; Jia, S.; Simpson, M. C.; Smith, K. M.; Fajer, J.; Shelnutt, J. A.; Holten, D. Picosecond to Microsecond Photodynamics of a Nonplanar Nickel Porphyrin : Solvent Dielectric and Temperature Effects. *J. Am. Chem. Soc.* **1998**, *120*, 3781–3791.

(29) Pegis, M. L.; Roberts, J. A. S.; Wasylenko, D. J.; Mader, E. A.; Appel, A. M.; Mayer, J. M. Standard Reduction Potentials for Oxygen and Carbon Dioxide Couples in Acetonitrile and *N*,*N*-Dimethylformamide. *Inorg. Chem.* **2015**, *54*, 11883–11888.

(30) Pegis, M. L.; Wise, C. F.; Martin, D. J.; Mayer, J. M. Oxygen Reduction by Homogeneous Molecular Catalysts and Electrocatalysts. *Chem. Rev.* **2018**, *118*, 2340–2391.

(31) Crabtree, R. H. Resolving Heterogeneity Problems and Impurity Artifacts in Operationally Homogeneous Transition Metal Catalysts. *Chem. Rev.* **2012**, *112*, 1536–1554.

(32) Artero, V.; Fontecave, M. Solar Fuels Generation and Molecular Systems: Is It Homogeneous or Heterogeneous Catalysis? *Chem. Soc. Rev.* **2013**, *42*, 2338–2356.

(33) Lee, K. J.; McCarthy, B. D.; Dempsey, J. L. On Decomposition, Degradation, and Voltammetric Deviation: The Electrochemist's Field Guide to Identifying Precatalyst Transformation. *Chem. Soc. Rev.* **2019**, *48*, 2927–2945.

(34) Wasylenko, D. J.; Rodríguez, C.; Pegis, M. L.; Mayer, J. M. Direct Comparison of Electrochemical and Spectrochemical Kinetics for Catalytic Oxygen Reduction. *J. Am. Chem. Soc.* **2014**, *136*, 12544–12547.

(35) Martin, D. J.; Mercado, B. Q.; Mayer, J. M. Combining Scaling Relationships Overcomes Rate versus Overpotential Trade-Offs in O_2 Molecular Electrocatalysis. *Sci. Adv.* **2020**, *6*, eaaz3318.

(36) Costentin, C.; Savéant, J.-M. Multielectron, Multistep Molecular Catalysis of Electrochemical Reactions: Benchmarking of Homogeneous Catalysts. *ChemElectroChem* **2014**, *1*, 1226–1236.

(37) Rountree, E. S.; McCarthy, B. D.; Eisenhart, T. T.; Dempsey, J. L. Evaluation of Homogeneous Electrocatalysts by Cyclic Voltammetry. *Inorg. Chem.* **2014**, *53*, 9983–10002.

(38) Currie, L. A.; Svehla, G. Nomenclature for Presentation of Results of Chemical Analysis. *Pure Appl. Chem* **1994**, *66*, 595–608.

(39) Savéant, J.-M.; Su, K. B. Homogeneous Redox Catalysis of Electrochemical Reaction. Part VI. Zone Diagram Representation of the Kinetic Regimes. *J. Electroanal. Chem.* **1984**, *171*, 341–349.

(40) Pegis, M. L.; McKeown, B. A.; Kumar, N.; Lang, K.; Wasylenko, D. J.; Zhang, X. P.; Raugei, S.; Mayer, J. M. Homogenous Electrocatalytic Oxygen Reduction Rates Correlate with Reaction Overpotential in Acidic Organic Solutions. *ACS Cent. Sci.* **2016**, *2*, 850–856.

(41) Pegis, M. L.; Wise, C. F.; Koronkiewicz, B.; Mayer, J. M. Identifying and Breaking Scaling Relations in Molecular Catalysis of Electrochemical Reactions. *J. Am. Chem. Soc.* **2017**, *139*, 11000–11003.

(42) Martin, D. J.; Wise, C. F.; Pegis, M. L.; Mayer, J. M. Developing Scaling Relationships for Molecular Electrocatalysis through Studies of Fe-Porphyrin-Catalyzed O_2 Reduction. *Acc. Chem. Res.* **2020**, *53*, 1056–1065.

(43) Groff, B. D.; Mayer, J. M. Optimizing Catalysis by Combining Molecular Scaling Relationships: Iron Porphyrin-Catalyzed Electrochemical Oxygen Reduction as a Case Study. *ACS Catal.* **2022**, *12*, 11692–11696.

(44) Harraz, D. M.; Weng, S.; Surendranath, Y. Electrochemically Quantifying Oxygen Reduction Selectivity in Nonaqueous Electrolytes. *ACS Catal.* **2023**, *13*, 1462–1469.

(45) Passard, G.; Ullman, A. M.; Brodsky, C. N.; Nocera, D. G. Oxygen Reduction Catalysis at a Dicobalt Center: The Relationship of Faradaic Efficiency to Overpotential. *J. Am. Chem. Soc.* **2016**, *138*, 2925–2928.

(46) Chang, C. J.; Loh, Z. H.; Shi, C.; Anson, F. C.; Nocera, D. G. Targeted Proton Delivery in the Catalyzed Reduction of Oxygen to Water by Bimetallic Pacman Porphyrins. *J. Am. Chem. Soc.* **2004**, *126*, 10013–10020.